Piezoelectric MEMS Accelerometers for Sensing Ossicular Vibration

by

Alison E. Hake

A dissertation submitted in partial fulfillment
of the requirements for the degree of
Doctor of Philosophy
(Mechanical Engineering)
in The University of Michigan
2021

Doctoral Committee:

Professor Karl Grosh, Chair
Professor Kenn Oldham
Professor Bryan E. Pfingst
Assistant Professor Serife Tol

Alison E. Hake

aehake@umich.edu

ORCID iD: 0000-0003-1161-7260

To Gilly, the dog who got me through grad school.

ACKNOWLEDGEMENTS

The work presented in this dissertation was generously funded by the National Science Foundation Graduate Research Fellowship Program (DGE 1256260) and by the Hearing, Balance, and Chemical Senses institutional training grant, NIH-NIDCD T32 DC000011.

When choosing a graduate school and advisor, I followed my gut and came to the University of Michigan to work with Dr. Karl Grosh. I have never regretted that decision. For six years, I have witnessed Dr. Grosh show sincere dedication to his students and immense enthusiasm for the projects we pursue. Thank you, Karl, for believing in me throughout this process and, most importantly, for your patience.

I would like to express many thanks to my committee members, Dr. Kenn Oldham, Dr. Bryan Pfingst, and Dr. Serife Tol, who have provided helpful assistance in the lab, access to experimental equipment, and insightful feedback on abstracts and presentations. Your expertise has been invaluable.

I have had the honor to work with and learn from many talented graduate students and postdocs in the Grosh Lab. For the transducer projects, there has been a consistent pattern of a senior graduate student mentoring the new student on the theoretical modeling and experimental testing of MEMS devices. To Dr. Chuming Zhao, thank you for passing along your knowledge and collaborating on these projects. Also, to Panagiota Kitsopoulos, the graduate student who will take over the transducer project, thank you for being an enthusiastic collaborator over the past year. Finally, I would like to thank Nathan Geib and Dr. Aritra Sasmal, who were great labmates but even better friends. Nate - thank you for brainstorming ideas and troubleshooting problems in the lab, but especially for letting me

vent for a while when frustration got the better of me. Ari - thank you for always being willing to drop what you were doing to answer my questions and help me through problems; you were so generous with your time.

I would also like to acknowledge and thank Ian Grosh and Sarah Chen. Ian spent a semester designing amplifier circuits for our experiments, and he also taught me how to use circuit design and analysis software and complete printed circuit board layouts. Sarah not only worked with me on the board layouts, but also tested the amplifier circuits and other electrical components in the lab. This behind-the-scenes progress was extremely important for the accelerometer experiments that I completed for this thesis.

I will be forever grateful to have met Dr. Maya Nath, Dr. Marie Rice Sasmal, Dr. Rachel Vitali, and Dr. Callan Luetkemeyer in grad school. These women are intelligent, hardworking, supportive, and kind, and they have inspired me in both academic and personal ways. Thank you all for your friendship and encouragement.

I would like to thank my parents, Richard and Kelly, and my sisters, Caylie and Emily, for supporting me with visits, phone calls, and packages of homemade cookies. Thank you for always believing in me. Finally, thank you, Dave, for your constant love and support. I would not have been able to do this without you.

TABLE OF CONTENTS

LIST OF FIGURES

Figure

LIST OF TABLES

Table

ABSTRACT

The structures comprising the human auditory periphery each perform unique functions to direct incoming sound, provide frequency-dependent gain, match impedance between air and liquids, and decompose the signal into its component frequencies. However, conductive and sensorineural hearing loss can significantly inhibit these functions, necessitating intervention to acquire or restore hearing capability. It is important to address hearing loss to avoid communication difficulties, cognition decline or hindered development, and social isolation. Technological solutions such as hearing aids, cochlear implants, and active middle ear implants have been developed to mitigate hearing loss. Despite the many historical successes of these devices, the externally-placed components still have significant drawbacks that have motivated research and development of completely-implantable sensing options. Not only do they require specific care and removal for certain activities (sleeping, bathing, exercise), but also necessitate signal processing to address feedback, improve microphone directionality, and reduce wind noise. An implanted system could function continuously and would utilize the outer ear for sound localization and protection from wind noise. The performance of implantable sensors must achieve all desired outcomes to outweigh the primary disadvantage - invasive implantation surgery. Therefore, the ultimate goal of this work is to advance completely-implantable auditory prosthesis systems through improved sensing capabilities.

In this work, we design a piezoelectric MEMS accelerometer as an ossicular vibration sensor. Piezoelectric sensing offers output linearity, low-noise material options, and the ability to interface the sensor with low-power circuits. To design the sensor, we first derive an analytic model. The analytic solution provides the full frequency response of the piezoelec-

tric beam to physical or electrical stimuli, but it does not readily allow for the observation of trends in the minimum detectable acceleration with dimension parameter changes. Hence, an assumed-mode model is used to obtain a closed-form solution of the minimum detectable acceleration of the sensor. With this model, we have enabled full design space analysis and can assess the influence of each design parameter on this key performance metric. Additionally, fabricated devices were tested experimentally to validate the analytic model.

In order to propose a design for this application, we map input sound pressure levels to acceleration values using ossicle vibration data from the literature. Based on hearing thresholds, we then set a minimum detectable acceleration design limit, which can be as low as 0.12 mm/s^2. Throughout the historical development of accelerometers for this purpose, the standard device design has a single resonance. However, with insights gained from this work, we conclude that a single-resonance accelerometer cannot meet the minimum detectable signal requirement across the entire frequency range in a small sensor die volume (less than 2.2 mm x 2.2 mm x 0.4 mm). Therefore, we propose a dual-resonant piezoelectric accelerometer design that incorporates two sensing elements, each with its own sensitivity and resonant frequency (i.e. functional bandwidth). This provides the necessary minimum detectable acceleration improvement over the low-frequency range, while the higher-resonance sensor maintains a wide bandwidth (8 kHz). The proposed sensor design can detect 20 phon equivalent acceleration levels from 100 Hz to 8 kHz. Modeled results also indicate that the proposed sensor design maintains a small die area (1.1 mm x 0.74 mm x 0.4 mm). Thus, the proposed design holds the potential to be the best-performing implantable ossicular vibration sensor in the literature.

CHAPTER I

Introduction

Humans are constantly immersed in a complex sound field in everyday life. Sounds in the environment caused by people, animals, traffic, and alarms must be sensed and interpreted for general understanding, to detect dangers, and to communicate with others. As these signals reach the ear, they are converted from the acoustic domain to structural vibrations to electrical signals in the brain. The structures comprising the auditory periphery each perform unique functions to direct sound, provide frequency-dependent gain, match impedance between air and liquids, and decompose the signal into its component frequencies. Various forms of hearing loss inhibit these functions and necessitate intervention to acquire or restore hearing capability.

In this introduction, we begin with a brief overview of the auditory periphery and its function for normal hearing, followed by an explanation of the types and severity of hearing loss and how it is measured. Technological solutions developed to mitigate the effects of hearing loss are mentioned to highlight shortcomings in the technology and motivate completely-implantable systems. The research on different sensing mechanisms for completely-implantable systems and the approach taken in this work are discussed, along with the specifications pertinent to sensor design.

1.1 The Auditory Periphery and Hearing Loss

1.1.1 Structure and Function of the Auditory Periphery

The human peripheral auditory system is shown in Fig. 1.1. Hearing begins at the outer ear, which has two main parts - the pinna (or auricle) and the external auditory canal (or ear canal). The cartilaginous pinna serves to direct incoming airborne sound pressure waves down the external auditory canal where they impinge upon the tympanic membrane [7]. The pinna provides some high-frequency filtering of the sound, and helps to distinguish whether the sound source is in front of or behind the listener [8]. Advantageously, a portion of the pinna, called the concha, and the ear canal resonate at approximately 2.5 and 5 kHz, respectively, providing natural amplification to the incoming sound [8, 9, 10]. The tympanic membrane terminates the internal end of the ear canal, separating the external environment from the internal middle ear cavity. It is a fibrous, toroidal and conic structure that is oriented at an angle with respect to the ear canal walls [11, 12]. Its shape, in conjunction with variable thickness and material properties, creates a complex vibratory pattern with many resonances [13], allowing for an efficient transfer of energy over a broad range of

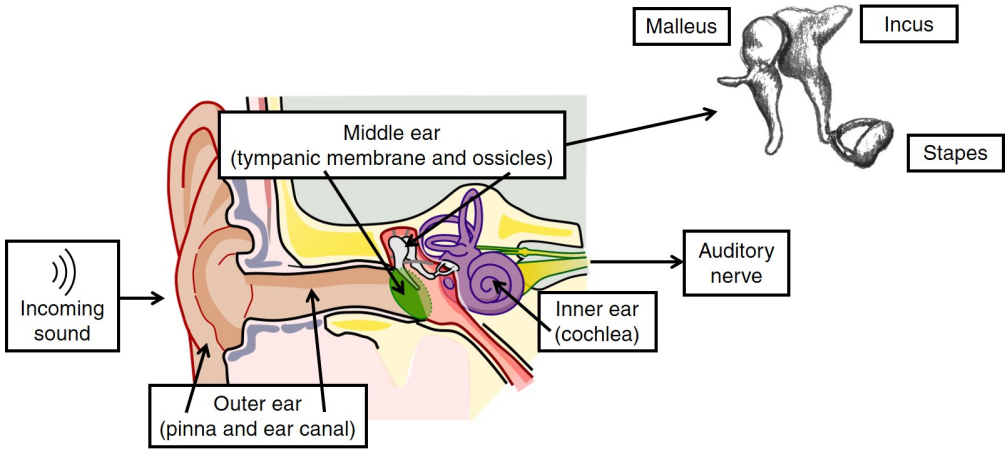

Figure 1.1: Diagram of the human outer, middle, and inner ear [1] with the primary parts labeled for reference. The pinna collects incoming sounds and directs them down the ear canal to the tympanic membrane. In the middle ear, the ossicles (malleus, incus, and stapes) vibrate and transmit the signal to the cochlea in the inner ear. The sketch of the ossicles is given for clarity and to label each bone.

frequencies from the outer to middle ear [12].

On the enclosed side of the tympanic membrane lies the middle ear cavity. The cavity is filled with air (when fluid from infection is not present) and is only open to the external environment through the Eustachian tube (opening for pressure equalization) [8]. Three ossicles - the smallest bones in the human body - called the malleus, incus, and stapes, are suspended by ligaments (the posterior ligament of the incus and the anterior ligament of the malleus) and muscles (the tensor tympani and the stapedius muscle) within the middle ear cavity (bones are depicted in Fig. 1.1). The malleus is firmly attached to the tympanic membrane at its top edge and at the vertex by the manubrium at the umbo [7, 12]. Between these two points, which are only a few millimeters apart [9], the membrane and the manubrium can be separated slightly in humans [12]. The head of the malleus joins the body of the incus at a double saddle joint and the ligaments attached to each bone keep the joint from separating [7]. The long process of the incus projects downward and connects to the head of the stapes at the incudostapedial joint [8]. The footplate of the stapes is attached to the oval window of the cochlea, where the signal is efficiently transferred to the fluid-filled ducts and other structures of the inner ear. The ossicular chain achieves impedance matching between the air in the ear canal and the fluid in the cochlea first by the decrease in surface area between the ear drum and the stapes footplate, resulting in a significant pressure increase [7, 9, 10]. Second, the lever action of the malleus and incus create a mechanical advantage to further aid in this transmission [7, 10]. All of these contributions in the middle ear system create a frequency-dependent transfer function that exhibits a maximum gain of 23.5 dB around 1.2 kHz [7, 8, 13, 14].

The inner ear is the most complex part of this system. The three main parts of the inner ear are the vestibule, the semicircular canals, and the cochlea which are situated in the temporal bone [7, 8]. The vestibule and semicircular canals comprise the vestibular system which is responsible for sensing changes in head motion, understanding spatial orientation, and maintaining balance and posture. The cochlea is a snail-shaped structure that contains

the organ of Corti, the sensory organ of hearing [9]. When the vibrating stapes moves the oval window, the fluid moves due to a pressure "release" at the membrane-covered round window. The fluid motion in the ducts, and the resulting pressure gradient, creates a traveling wave that deflects the basilar membrane, a structure that supports the sensory hair cells [10, 15]. The hair cells have rows of stereocilia which move in response to fluid motion, opening mechanoelectrical transduction channels and sending electrical signals to be perceived as sound in the brain. As the structure of the basilar membrane changes along its length, the maximum excitation for a particular frequency corresponds to a specific place [9, 10]. In this way the cochlea exhibits a tonotopic map with high frequencies close to the oval window (base of the cochlea) and low frequencies at the end of the spiral shape (apex of the cochlea).

The process of sound transmission described up to this point is called air conduction hearing, but this is not the only way to stimulate the cochlea. Acoustic signals can also be perceived through bone conduction hearing where incoming sound vibrates the bones of the skull. There are two subsets of bone conduction hearing that are distinguished by the stimulation frequency, inertial and compressional [7]. At low frequencies (below about 1.5 kHz), the skull moves as a rigid body and the ossicles move relative to the skull due to their inertia. This results in the previously described cochlear response to oval window motion. At higher frequencies, where the bones of the skull are responding in complex mode shapes, the cochlea may be directly compressed (since it is surrounded by the temporal bone) [16]. The round window membrane moves in response to the compression and the fluid is able to move within the ducts and stimulate hearing.

1.1.2 Hearing Loss: Types, Severity, and Measurement

In the United States, bilateral (both ears) hearing loss affects at least 13% of people age 12 or older [17] and increases to 23% for unilateral (one ear) hearing loss [18]. While disabling hearing loss can be experienced at all ages, its prevalence increases as people age [19]. The two primary types of hearing loss are conductive hearing loss and sensorineural hearing loss [3].

A third category, mixed hearing loss, arises as the combination of the two types. Conductive hearing loss refers to a disruption in the air-conduction hearing pathway; essentially, the sound and vibration cannot be transmitted to the inner ear, or it is transmitted at amplitudes significantly lower than the threshold that can be detected in the cochlea. Conductive losses can be caused by outer ear obstructions (wax), infections and trapped fluid in the middle ear, perforation of the ear drum, dislocation of the ossicles, or abnormal bone growth (otosclerosis) [15, 20]. Sensorineural hearing loss results from hair cell damage or natural degradation within the cochlea that inhibits the mechanoelectrical transduction required to sense the sound. This can occur over all frequencies (damage throughout the entire cochlea) or over a range of frequencies (localized damage). Sensorineural hearing loss is often the result of aging, but also can be caused by heredity, infections, prolonged noise exposure, or trauma [2, 20]. The severity of either type of hearing loss can range from mild cases where it has become difficult to hear soft sounds to profound cases where sounds must be very loud to be audible. It can also vary with frequency and can even change over time.

Hearing tests are used to identify and characterize the level and frequency-dependence of an individual's hearing loss. Periodic testing also demonstrates how one's hearing threshold changes as they age. One such hearing assessment is pure-tone audiometry. During this test, as the name suggests, pure tones ranging in frequency from 125 Hz to 8 kHz are presented to a patient through headphones (air conduction) or with a bone conduction device [2, 3, 7]. The intensity level at which the patient can reliably detect the presented sound is compared to the normal hearing threshold of a healthy-hearing population (measured in decibels hearing level, dB HL) [2]. Test data is presented graphically for both ears with air and bone conducted stimulation in an audiogram. Figure 1.2 shows an example of an audiogram wherein air-conduction data are conventionally marked with circles; for the sake of simplicity, only one data set is shown here. The tested frequencies are plotted on the x-axis and the threshold value is plotted on the y-axis (with increasing positive values downward). This example plot also includes shaded ranges of dB HL values indicating the severity of hearing loss that

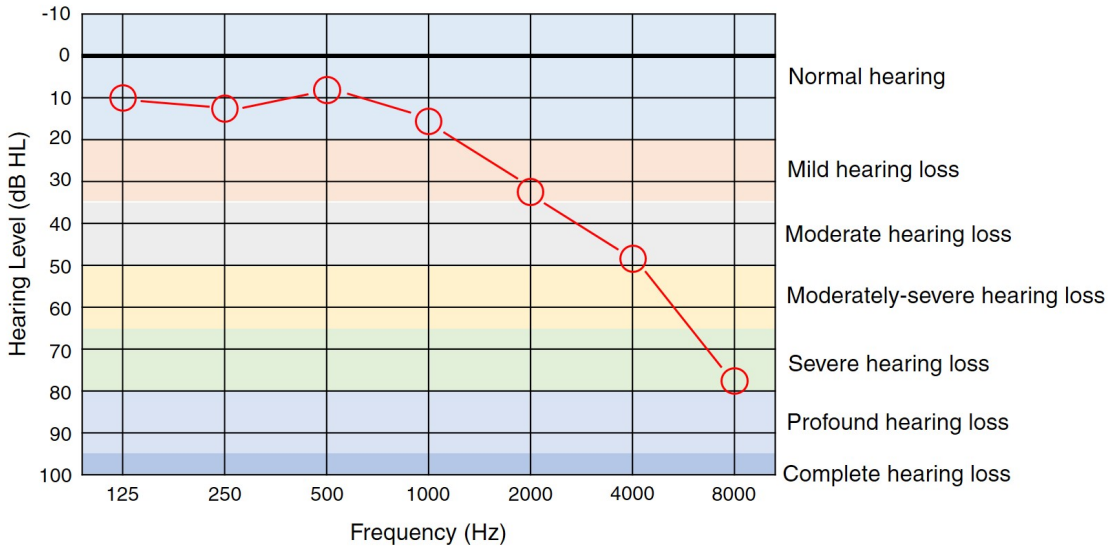

Figure 1.2: Conceptual example of an audiogram. Red circles indicate the measured threshold of the pure tone stimulation frequency for air-conducted sound in a single ear. Additional data are typically included for bone-conducted test signals and for the left ear, but are omitted for simplicity. Shaded regions demonstrate the hearing level ranges, measured in dB HL relative to a healthy hearing threshold), for various severities of hearing loss. This diagram does not include real data, and was not directly recreated from any source, but was influenced by open-source images and examples in [2, 3].

would typically be experienced with each dB HL [3].

With the information provided in an audiogram, an audiologist can assess important aspects of the hearing loss. They will determine if the hearing loss is the same or different in the left and right ears and distinguish the type(s) of hearing loss present. For instance, sensorineural hearing loss is indicated by the same air and bone conduction threshold levels at each tested frequency. On the other hand, if they are different, particularly if the bone conduction threshold is lower than air conduction threshold, the individual is likely experiencing conductive hearing loss [2]. The audiogram highlights other hearing loss characteristics as well, such as the increasing threshold with increasing frequency trend typical to age-related hearing loss (such as the example shown in Fig. 1.2). Other hearing tests, such as tympanometry, auditory brainstem response (ABR), and otoacoustic emmissions, can be used to further interrogate the causes of hearing loss. These examinations are also appropriate for small children or others who cannot respond to complete the pure-tone audiometry [7].

Once the hearing loss is identified and quantified, it is important to address it with medical, surgical, or technological interventions. Studies have demonstrated that neglecting hearing loss in adults may result in social isolation, difficulties communicating, and has detrimental affects on cognition [2, 3]. In children, hearing loss negatively impacts cognitive development, speech, and learning [3]. Medications can be used to resolve cases of infection or middle ear fluid, leading to restored hearing levels. Conductive hearing losses involving tympanic membrane perforations or otosclerosis may necessitate surgical procedures to fix the perforation or to implant passive ossicular chain prostheses to improve hearing. Sensorineural hearing loss and cochlear damage, on the other hand, cannot be fixed my surgery or medicine (although development of drugs and therapies for this purpose is an active area of research [21]). It is addressed with technological solutions such as hearing aids and cochlear implants that amplify the incoming sound to stimulate the hair cells at a higher level or bypass the sensory cells and directly electrically stimulate the auditory nerve. These technologies and their shortcomings will be discussed in the next section.

1.2 Technological Solutions for Hearing Loss

1.2.1 Hearing Aids

For the sake of completeness in this discussion, it is important to mention that there are two sub-categories of hearing aids (HAs) - acoustic HAs and bone conduction HAs. Acoustic HAs stimulate hearing with amplified sound through the air conduction hearing pathway, whereas bone conduction HAs stimulate the bone conduction pathway. Bone conduction HAs sense and process incoming acoustic sounds, then drive a transducer that is anchored to the skull to induce vibration [22]. Aside from noting that the external components of this system and anchoring method may require specific care or cause issues that motivate the transition to completely-implantable systems, we will not be discussing the literature surrounding these devices in this introduction.

With an acoustic HA, environmental sounds are sensed with a microphone (or array of microphones), the signals are digitally processed and amplified according to the needs of the user, and then a receiver (specifically an acoustic speaker) is driven with the conditioned signal [4]. The components of this system are arranged/housed in several different externally-placed configurations, as demonstrated in Fig. 1.3. For example, the microphone, processor, and speaker can be housed in a single case that is molded to fit in the ear at the canal opening or to be inserted deeper within the ear canal (images (a) and (b)). Alternatively, the sensor and signal processor can be packaged and placed in a housing behind the ear while the receiver is placed in the ear canal with a dome fitting to hold it in place (such as (c) or (d)) [4]. The choice of device style depends on many user-dependent diagnostic and experiential factors.

In general, acoustic HAs are used to treat mild to moderate hearing loss. Mild/moderate cases necessitate practical levels of amplification from the signal processors and driven speakers to overcome the increased hearing threshold. If the hearing loss worsens, requiring increased signal gain for audibility, the possibility of acoustic feedback also increases. Although, the trade-off between achievable gain and acoustic feedback exists for HAs, regardless

Figure 1.3: Images of different hearing aid styles. (a) and (b) demonstrate in-the-ear and in-the-canal type HAs. Behind-the-ear systems are shown in (c) and (d). This image is reused by permission from: *Hearing Aids*, Springer Handbook of Auditory Research, Springer International Publishing Switzerland 2016 [4].

of stimulation levels. Oftentimes, feedback can be eliminated by reducing gain at problem frequencies, testing a style in which the microphone and speaker are spaced farther apart, or using tighter-fitting molded earpieces (less sound leakage) [23]. For receivers secured in the ear canal with dome fittings, vent hole size is another variable that can be adjusted to address this issue. However, another design/functionality trade-off arises because tighter fitting molds and reduced venting can lead to noticeable occlusion effects, especially if the user has milder hearing loss at low frequencies than at high frequencies [23].

Signal processing strategies such as digital feedback suppression or occlusion-specific programs are also successful without physical device changes [23]. Additional algorithms are implemented for frequency-dependent signal compression, microphone directionality or beamforming, noise and reverberation cancellation, wind noise reduction, and environmental classification, among others [4]. Many of these signal processing strategies - particularly those for feedback, occlusion, directionality, and wind noise - would become obsolete with a completely implanted system. There would no longer be a device in the ear canal causing occlusion, irritation, or infection. Furthermore, the (extremely variable [24]) acoustic feedback path would be eliminated without the combination of a microphone and speaker in close physical proximity. Finally, the system would take advantage of the pinna and ear canal which contribute to determine signal directionality and block wind noise from affecting the ear drum.

Modern devices have incorporated advanced signal processing strategies and extra functionality to be compatible with electronics (such as Bluetooth connectivity to cell phones) [23]. However, still only 16% of 20 to 69 year-olds and 30% of people 70 and older who could benefit from using HAs have actually adopted the technology [19]. The low uptake is likely due to many of the aforementioned factors as well as the patience required to endure iterations of physical fitting procedures and adjustments to the many electrical parameters to achieve optimal function. While some tuning of the signal processing would still remain for a completely-implantable system, eliminating stigma and the need to care for small external

components could benefit many HA users.

1.2.2 Cochlear Implants

Cochlear implants (CIs) bypass the air and bone conduction hearing pathways and stimulate the auditory nerve directly [3, 25]. Current CI systems consist of both external and internal components, illustrated in Fig. 1.4 (behind-the-ear style shown). The microphones and signal processors are contained in behind-the-ear or off-the-ear external housings [25]. The behind-the-ear housing is wired to an inductive link that transmits the digital signal to the implant below the skin [26, 27]. This portion of the system is secured magnetically, as are the off-the-ear style processors (that also contain the inductive signal transmission in the same component). Acoustic signals detected by the microphones are processed into frequency bins according to spectral content, then sent to the internal receiver that is connected to the implanted electrode array [27]. The dedicated frequency range for each electrode corresponds to the particular cochlear location that is being stimulated with electrical pulses (recall the tonotopic place-frequency map). According to the National Institute on Deafness and Other Communication Disorders, over 180 thousand adults and children in the United States have a CI [19]. In order to justify surgical implantation of a CI, the case of sensorineural hearing loss should be severe or profound. In these instances, even high gains through a HA would

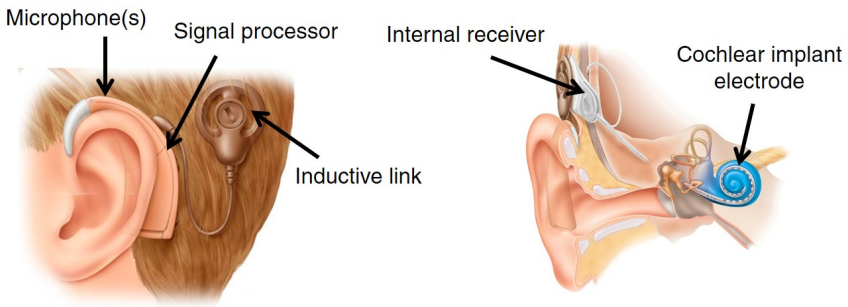

Figure 1.4: Illustration of the external and internal parts of a cochlear implant (CI). The microphone(s) and signal processor are located in a behind-the-ear housing; outputs are connected to an inductive link that transmits the signal to an internal receiver. The receiver stimulates the implanted cochlear electrode based on the frequency content of the incoming sound. (Images: BC Family Hearing, CC BY 4.0 [5])

not be enough to stimulate hearing, at least not before causing feedback or saturating the capabilities of the hardware (speakers) [3]. Therefore, direct electrical stimulation is more appropriate.

Considering the use of external microphones and signal processing units, many of the same challenges facing HAs are translated to CIs, except for acoustic feedback and ear canal occlusion [27, 28]. Additional signal processing algorithms could be eliminated with a completely-implantable system that experiences a natural representation of hearing though the outer and middle ear. Furthermore, the external components have some physical drawbacks, which are also pertinent to HAs. The signal processor, or the entire HA, may need to be removed during sleeping or rigorous exercise, and if it is not waterproof, also during bathing or swimming [29, 30]. The lack of 24/7 functionality causes safety concerns, particularly for the level of hearing loss addressed by CIs. Clearly, complete implantability will improve CI systems and benefit CI users as well.

1.2.3 Active Middle Ear Implants

In the effort to bridge the gap between HAs and CIs, especially in cases of mid-range hearing loss, systems called active middle ear implants (AMEIs) were developed [31]. These devices aim to eliminate externally-worn, in-the-canal components of HAs, but some retain behind-the-ear processors with microphones for sensing. Internally, electromagnetic or piezoelectric transducers drive the motion of the ossicles or the round window of the cochlea to stimulate hearing at an amplified level, which allows the cochlea to remain undisturbed surgically [32]. Despite these advantages offered by AMEIs, the primary disadvantage of this approach is the need for invasive implantation surgery even when an electrode is not implanted in the cochlea (accompanied by the potential need for revision surgeries and irreversible changes within the middle ear cavity). The long history and progression of AMEIs will not be recounted here, but the interested reader can find detailed reviews on the topic [31, 32, 33]. However, three systems should be highlighted owing to their "complete

implantability" - the totally implantable cochlear amplifier (TICA, purchased by Cochlear Ltd., Sydney, Australia in the early 2000s [32]), the Carina (also now owned by Cochlear Ltd., Sydney, Australia), and the Esteem (Envoy Medical Corporation, White Bear Lake, MN, USA). The references that follow in this section provide detailed diagrams and photographs of these and other devices.

The TICA was the first completely-implantable device. Implantability was achieved placing the sensing microphone under the skin in the ear canal near the tympanic membrane [31, 33]. Sensed signals are processed and used to drive an internal piezoelectric actuator that can be attached to the incus or stapes footplate. Despite utilizing the natural functional benefits of the pinna and ear canal at the chosen microphone location, issues of noise feedback arose due to the actuator-driven tympanic membrane motion [32, 33]. Malleus resection to decouple the ossicles resolved the feedback issue, but also created conductive hearing loss that must be addressed in the event of device explantation.

The Carina system was changed from semi-implantable to fully-implantable with the inclusion of a subcutaneous microphone placed behind the ear [33]. Microphone signals are sent to an internal receiver and processor that drive an electromagnetic transducer; the transducer can be connected to the incus body, stapes, oval window, or round window by various specialized attachments [34]. Since the microphone is far from the ear canal, there is no risk of acoustic pick-up from the driven ossicle motion; thus, disarticulation is not required. However, since it is located beneath the skin, the microphone is sensitive to changes in tissue thickness that can occur naturally over time or may be short-term changes as a result of head or neck movements [35, 36]. Noise from these movements will be detected and processed, and other body noises may interfere with daily listening though this device. This system also neglects the pinna and ear canal functions that would benefit the incoming signal.

The Esteem system is comprised of two implanted piezoelectric transducers, one to detect motion of the body of the incus, and one to drive the head of the stapes [32, 33, 34].

To eliminate feedback from the stapes driver, the long process of the incus must be cut to disrupt the ossicular chain [33]. Similar to the TICA, this hinders the reversibility of Esteem implantation. However, the implanted transducers are effective sensors and actuators, and the system provides constant hearing through the natural filters of the pinna and ear canal [31, 36]. In some cases, the transducers and signal processor are too large to be implanted. Decreasing the sensor size may increase the applicability of this technology to more patients.

As evidenced by these completely-implantable AMEIs, implantation by way of subcutaneous microphone is not as effective as sensor placement in the middle ear. There are ongoing research efforts to alter the size and attachment scheme of the ossicle motion sensor, or to employ a different method of sensing altogether. Some of this sensor-focused research is discussed in the next section.

1.2.4 Sensors for Completely Implantable Systems

The sensor, signal processor, and actuator (be it a physical or electrical stimulator) must all be carefully designed to enable a completely-implantable auditory prosthesis and justify the risks associated with surgery. The sensor must be able to detect all of the necessary information so that the signal processor can drive the actuator in the most effective way possible. While the external placement of microphones in HAs and CIs is not ideal, these microphones are high-performance sensors with high sensitivities, low noise floors, and wide frequency and dynamic ranges [37]. Therefore, approaches including commercially designed, high-performance microphones have been attempted.

Two commercial microphone approaches will be highlighted here. First, a trans-tympanic approach is taken whereby a ventilation tube (commonly used to treat otitis media) is connected to the inlet port of an electret microphone implanted in the middle ear cavity [38]. This concept is stated to have minimal impact on the normal vibration of the tympanic membrane, however some downsides to this approach include possible wax obstruction of

the tube, migration of the ventilation tube into or out of the tympanic membrane, and requiring care to prevent fluid from entering the tube. Second, out of the same research group, is a vibro-acoustic hybrid sensor that incorporates a microphone to sense acoustic signals transmitted through the tympanic membrane and an accelerometer to detect ossicle vibration [39]. While the results of this work are promising (the microphone does indeed aid in extending the frequency range of the system), there is no discussion concerning protective diaphragms for the microphone. This will be necessary to prevent moisture or fluid from degrading the microphone performance or damaging the sensor, and will inherently affect microphone performance. Microphone degradation aside, the sensor may pick up undesirable body-generated sounds reaching the middle ear cavity by bone conduction in this type of system.

An alternative to pressure detection in air within the middle ear cavity is pressure detection in fluid within the cochlea. This is an attractive sensing mechanism because the input signal will have been shaped by both the outer ear and the middle ear transfer functions. The first device to mention is a natural transition from the previous two devices - it is called the intracochlear acoustic receiver (ICAR) [40, 41]. In this system, a high-end commercial microelectromechanical systems (MEMS) microphone is protected by a specially designed titanium enclosure which is partially inserted in the cochlea. Next, pressure sensors designed to directly interact with the cochlear fluid have been designed in our group and by others. Knisely, Zhao, and Grosh developed piezoelectric cantilever arrays called the completely implantable artificial organ of Corti (CIAO) or the piezoelectric implantable acoustic transducer (PIAT) [30, 42, 43, 44, 45]. The cantilevers on these sensors have different resonances to be more sensitive to certain frequency stimuli, but they are fabricated on a rigid backbone that cannot flex around the turns of the cochlea. On the contrary, Creighton, *et al.* and Park, *et al.* created a flexible, silicone and piezoelectric polymer sensor for this purpose, but the device geometry has a single frequency response to incoming pressure [46, 47]. All of these works have shown successful experimental proof-of-concept for these devices, but it

has yet to be determined how these devices will work in conjunction with, or instead of, an implanted stimulation electrode.

Finally, MEMS accelerometer designs have been studied for more than 20 years in the effort to overcome electrical noise limitations and achieve the bandwidth required for this application [48, 49, 50, 51, 52, 53, 54]. Similar to the Esteem system, a MEMS accelerometer measures vibration by contact with an ossicle; however, rather than being anchored in the wall of the middle ear cavity and contacting the bone at a point, it is placed directly on the ossicle. This simpler attachment scheme may be advantageous for surgical implantation and to eliminate necessary healing of internal tissue. Furthermore, attaching the accelerometer to an ossicle accounts for the effects of the outer and middle ear on the incoming signal. Unlike microphones, MEMS accelerometers can be packaged and protected from the environment without performance degradation. With advances in MEMS microfabrication, especially in regard to depositing high-quality piezoelectric films, acceleration sensing is a promising path forward for completely-implantable hearing systems.

1.3 Piezoelectric MEMS Accelerometer Approach

1.3.1 Benefits for Implantable Auditory Prosthesis Applications

In this work, we present a MEMS piezoelectric accelerometer design for this application. Piezoelectric sensing offers several conveniences and advantages. First, piezoelectric sensors behave linearly over a wide range, as opposed to capacitive sensing which is limited by small gaps between electrode faces [55]. Next, with modern microfabrication techniques, piezoelectric sensors can be made of materials such as aluminum nitride (AlN) or scandium-doped AlN that have low dielectric loss properties (i.e. they are low-noise) [56].

Power consumption is a key factor in the success of completely-implantable systems. Although a specific focus on designing a low-power system is outside the scope of this work, we are confident that this sensor can inherit low-power circuit design strategies (resulting in

roughly tens of μW consumed) used for piezoelectric sensor inputs as seen in the literature [57, 58, 59] and with commercial sensors [37]. Furthermore, since piezoelectrics intrinsically generate a voltage in response to applied load they do not require a charge pump to develop a bias voltage. Therefore, there is greater flexibility in creating power saving cycling algorithms (e.g., startup times are much smaller without a charge pump).

Unfortunately, commercial MEMS accelerometers do not offer a convenient plug-and-play solution. Despite being meticulously designed for use in consumer electronics, inertial measurement units, and wearable activity monitors, many of the low-noise and low-power options also have a narrow bandwidth. For instance, packaged MEMS accelerometers with digital outputs from Bosch Sensortec such as the BMA456 are conveniently small (2 mm x 2 mm x 0.65 mm) and consume little power, but the bandwidth of the sensors is only 1600 Hz (limited by the output data rate) [60]. Another example, the TE Connectivity Model 820M1 piezoelectric accelerometer, has a large bandwidth (up to 10 kHz) but the packaged dimensions are nearly 9 mm x 9 mm [61]. Recently, MEMS accelerometers for detecting voice through bone conduction vibration have been manufactured and incorporated into headphones. One particular example is the Vesper Technologies VA1200, which comes in a small package (2.9 mm x 2.76 mm x 0.9 mm), but resonates at 2.8 kHz so the usable bandwidth only reaches about 2.4 kHz [62]. While this is not an exhaustive list of accelerometers on the market, these examples demonstrate that the specific combination of design requirements for this application is unique. Therefore, a new sensor must be designed with all of the requirements in mind from the start; the criteria for measuring the vibration of ossicles in the middle ear are discussed in the next section.

1.3.2 Sensor Specifications for Measuring Ossicular Vibration

To use a MEMS accelerometer to sense middle ear motion, several stringent (and often conflicting) physical and electrical requirements must be met. First, the middle ear space is highly constrained; the packaged sensor must have small linear dimensions to be securely

attached to a half-centimeter sized ossicle [8]. In our experience, approximately 3 mm long or wide is possible to fit on the manubrium of the malleus at the umbo, but the height of the device should not exceed approximately 1 mm. Even with these guidelines, the available space in any middle ear will vary; a volume up to about 22 mm^3 can be used, but may require removal of the incus [39, 49, 63]. If the long process of the incus is chosen as the attachment location, then the volume has been demonstrated to increase to nearly 90 mm^3 [52]. However, such large volumes also have large masses. The device from Jia, *et al.* in particular is 67 mg [52], which is more than twice the average mass of the incus (approximately 30 mg [8]). Large linear and rotational inertia are more likely to adversely affect the vibration of the ossicular chain, making the signal more difficult to detect and hindering the transmission of signals where there may be residual hearing. Other research groups have found that middle ear sensors with masses on the order of tens of milligrams (25 mg [50] and ∼50 mg [39], for example) have had minimal effect on ossicular motion, so this mass range serves as an order of magnitude benchmark. Nevertheless, decreasing the mass as much as possible and testing inertial-loading effects based on implantation location will still be needed.

HA or CI microphones provide a sufficiently large usable frequency range and input dynamic range that should be emulated with the implanted accelerometer. These acoustic sensors typically have a usable bandwidth of 0.1-10 kHz and an 80-90 dB dynamic range [37, 64] closely corresponding to the 70-100 dB dynamic range of human hearing [6, 63]. For the accelerometers, the frequency range does not have to be quite as generous; anything wider than 100 Hz - 8 kHz is sufficient to detect frequencies important to speech while neglecting body motion sounds below 100 Hz [63].

In previous reviews and discussions about the accelerometer requirements, the minimum detectable signal was specified as a constant sound pressure level across the desired frequency range, specifically 40 dB SPL [63]. However, that definition does not take into account the frequency-dependence of hearing or utilize the frequency-dependence of the sensor minimum

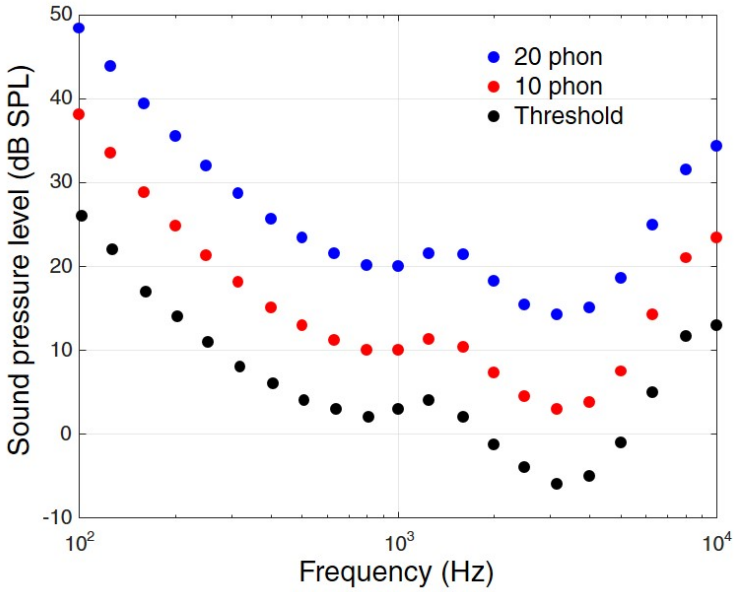

Figure 1.5: Average dB SPL values of the hearing threshold and two equal-loudness-level contours (10 and 20 phon). Hearing threshold data points (black), and 10 phon (red) and 20 phon (blue) data points are estimated or taken directly from BS ISO 226:2003 [6]. The 20-phon contour will represent the minimum detectable signal specification for the accelerometer.

detectable signal (this will be discussed in Chapter II). Hence, we aim for a requirement that is defined by the threshold of hearing so that the sensor can detect and process low-level input signals. The average dB SPL values for the hearing threshold are plotted with black points in Fig. 1.5. Two equal-loudness-level contours are also plotted; the 10 phon (red points) and 20 phon (blue points) contours illustrate the sound pressure levels that are perceived to be as loud as a 10 or 20 dB SPL 1 kHz reference signal. These data are found in BS ISO 226:2003 [6], given as table values for the 10 and 20 phon contours and estimated from the plot in Annex A for the hearing threshold values. Interestingly, the 20 phon contour is approximately 20 dB greater than the threshold level across much of the frequency range. Therefore, since hearing loss is measured relative to the normative threshold, using the 20 phon contour as the requirement will result in normal hearing or mild hearing loss level functionality to the implanted person. The conversion from sound pressure level input to equivalent ossicle acceleration will be discussed later in Chapter III.

Previous research has been undertaken to develop an accelerometer to meet these requirements. Capacitive accelerometer embodiments, such as those presented by the Ko group [49, 50] and Sachse, *et al.* [51] do not meet the bandwidth requirement nor do meet the 20 phon detectable signal specification over tested frequencies. A hybrid microphone-accelerometer design proposed by Seong, *et al.* [39] has a slightly improved signal-to-noise ratio compared to Ko, *et al.* [49], but still cannot detect the lowest desired signals. Park, *et al.* [48] created a very small piezoresistive device, but the lower limit of the bandwidth is 700 Hz and the minimum detectable signal much higher than the 20 phon equal-loudness-level contour across the entire frequency range. Piezoelectric sensors have been designed by Jia, *et al.* [52], and Gesing, *et al.* [53, 54], but none meet the minimum detectable signal requirement (especially at low frequencies) nor do they cover the full bandwidth of interest. While considerable progress has been made in the area of acceleration sensors, none of these sensors yet meets the minimum detectable signal requirement over the desired acoustic bandwidth for implementation in an implantable auditory prosthesis.

1.4 Overview and Organization

Overall, the work presented in this dissertation has followed a design-build-test-iterate approach. The ultimate goal of this work is to advance completely-implantable auditory prosthesis systems through improved sensing capabilities.

In Chapter II, the analytic model of the proposed MEMS piezoelectric bimorph accelerometer is discussed in detail. The model begins with uniaxial stress constitutive assumptions that are used to derive a minimum detectable acceleration design equation. In this process, it is found that the design equation trends indicate that the piezoelectric beams should be much wider than is valid for the original assumptions. A plane-strain constitutive hypothesis is used to derive and test equivalent material properties; a full 3-dimensional finite element model confirms that the wider structures are more accurately modeled with the plane-strain hypothesis. Regardless of the hypothesis used, the design equation is still

valid and is used to quickly assess the design space without requiring lengthy finite element simulations. Case studies using the minimum detectable signal expression demonstrate its use in a non-application-specific context.

Chapter III includes the experimental testing of the first fabricated accelerometers. These devices were fabricated in a collaboration with Vesper Technologies; therefore, our designs were constrained to their processes and available MEMS die space. Rather than use the derived design equation with the applied constraints, we chose conservative dimensions to ensure yield of functional sensors. Ideally, each step in a fabrication process will be tuned so that the resulting geometry matches the as-drawn design. Since we did not have control over the process in this case, we identify that the proof mass is under-etched, meaning that it is larger than the designed dimensions. The fabricated devices undergo material property and sensor performance characterization testing, and the results are presented for a tested beam. Measured and data-fit parameters indicate that the deposited AlN films were of good quality. The results also demonstrate that the analytic models are valid for devices that are subject to realistic fabrication variability. Ultimately, the work in this chapter elucidates that this piezoelectric accelerometer configuration with a single device resonance will not achieve the all of the requirements for implantation and sensing in the middle ear.

Based on these results, a new concept is proposed in Chapter IV. In theory, many of the design variables for this system can be independently controlled for a single beam that is electrically connected to other specially-designed beams. This approach is explored to understand if it is possible to simultaneously increase the sensitivity and bandwidth of the sensor by adding beam outputs of differing sensitivity and resonant frequency in phase with each other. The modeled results demonstrate that this is indeed possible. In addition, an alternating phase case shows that a band-pass region of higher sensitivity caused by the beam resonant peaks can be achieved. Although these are interesting ideas, the number of beams required to generate a smooth sensitivity spectrum is expected to be high, and the fabrication processes become increasingly complicated when for varying beam and mass

dimensions. Scaling back this concept to fewer beams and a different approach to obtain the desired sensitivity output, we consider a dual-resonant accelerometer. Two piezoelectric beams are designed to meet the requirements for minimum detectable acceleration over independent frequency ranges within the application bandwidth. The chapter concludes with a proposed design that would be, to our best knowledge, the best-performing implantable ossicle vibration sensor for auditory prostheses in the literature.

CHAPTER II

Modeling the Piezoelectric Accelerometer

This chapter discusses the mathematical modeling of piezoelectric elements, particularly in response to bending, as well as their connections to each other in sensing systems. The accelerometer model builds on the body of work developed for layered piezoelectric cantilevers by researchers in the Grosh Lab over the past decade [30, 45, 55]. The model presented here will be used for the sensors in Chapters III and IV, with any specific additions or changes indicated in those chapters.

The full analytic solution for the sensitivity, actuation response, noise, and minimum detectable acceleration are given, as well as an assumed mode solution that results in low-frequency design expressions for the system. The use of the design equation is demonstrated with two approaches in a case study. Finally, a brief comparison of the analytic model results to a finite element model solution highlights differences in the constitutive hypotheses that are used to model these piezoelectric beams.

2.1 Introduction

Electromechanical transducers convert energy to or from the mechanical and electrical domains. In devices such as microphones, speakers, motors, or accelerometers the conversion occurs through capacitors, magnets and coils, and piezoelectric materials, among other methods. Since the discovery of piezoelectricity in the late 1800s, through the search for naturally

occurring and man-made piezoelectric materials in the mid-1900s, and due to modern-day inclusion of piezoelectric thin films in microfabrication processes, piezoelectric media are commonly used for electromechanical transduction [65].

The piezoelectric effect occurs naturally in quartz, tourmaline, and Rochelle Salt (potassium sodium tartrate tetrahydrate) based on the lack of central symmetry in the material's crystal structure [65]. In these crystals, an electric dipole is generated when a stress/strain is applied in one or more particular crystallographic orientations. Conversely, an applied electric field will cause material strain. Transducers made of these materials must be precisely cut to take advantage of the piezoelectric effects. Dipoles also exist naturally in ferroelectric polycrystalline materials such as lead zirconate titanate (PZT) or barium titanate at temperatures below the Curie point where the material phase forms a tetragonal structure. However, they are randomly oriented within the material and must be aligned to create a bulk piezoelectric response [66]. Once the material is formed into the desired shape (by sintering or other processes), and electrodes are applied to opposing parallel surfaces, it can be poled. The poling process requires a strong, constant electric field applied across the electrodes that is held for a period of time at raised temperatures. The dipoles within the material will nominally reorient in the direction of the applied electric field. Non-ferroelectric materials do not respond to this type of poling process; rather, they must be deposited or grown in the proper orientation to align the polar directions and function as a piezoelectric material [66]. As piezoelectric materials have been incorporated into MEMS devices, thin film deposition techniques such as sputter deposition are used to achieve poled piezoelectric films with good properties [67].

Whether the material is poled or grown in a particular orientation, the polar axis of the piezoelectric material is conventionally assigned the 3-coordinate (considering a Cartesian coordinate system where the 3-axis is perpendicular to the 1-2 plane). Ferroelectric or non-ferroelectric thin films have in and out-of-plane piezoelectric responses, as described by the piezoelectric coupling equations that can account for any direction of applied physical or

electrical stimuli [55, 65, 66]. Different forms of the coupling equations depend on the choice of dependent and independent variables, and the material property coefficients used will change accordingly. For instance, the strain-charge form of the coupling equations has strain (ε) and electric displacement (D) as dependent variables, with stress (σ) and electric field (E) being independent variables. The general strain-charge form is the following set of equations:

$$[\varepsilon] = \boldsymbol{s}^{\boldsymbol{E}}[\sigma] + \boldsymbol{d}^{\boldsymbol{t}}[E] \tag{2.1}$$

$$[D] = \boldsymbol{d}[\sigma] + \boldsymbol{\epsilon}^{\boldsymbol{\sigma}}[E] \ . \tag{2.2}$$

The matrices $\boldsymbol{s}^{\boldsymbol{E}}$, $\boldsymbol{d}$, and $\boldsymbol{\epsilon}^{\boldsymbol{\sigma}}$, indicated in bold font, are the elastic compliance measured under constant electric field, piezoelectric coefficient, and permittivity measured under constant stress, respectively. $\boldsymbol{d}^{\boldsymbol{t}}$ denotes the transpose of the piezoelectric coefficient matrix.

Conveniently, poled or oriented piezoelectric films have a particular symmetry (dihexagonal polar class with in-plane isotropy [55]) that reduces the number of non-zero material constants in the matrices above. The remainder of this chapter will focus on modeling the direct and inverse piezoelectric response of beam structures with particular constitutive assumptions and specific electrical/mechanical boundary conditions.

2.2 Preliminaries of Piezoelectric Beam Sensing and Actuation

2.2.1 Direct and Inverse Piezoelectric Effect with Bending Elements

As mentioned above, the piezoelectric coupling equations describe the physical and electrical responses for the direct piezoelectric effect and the inverse piezoelectric effect [68]. These scenarios are depicted for beam elements in Fig. 2.1. First, panel (A) shows a beam element with electrodes on the top and bottom surfaces that is subjected to a distributed force (stress) in the 3-direction causing the material to be strained. As a result or the direct piezoelectric effect, a proportional charge is generated on the top and bottom electrodes, where positive or negative charge depends on the polarity of the piezoelectric material.

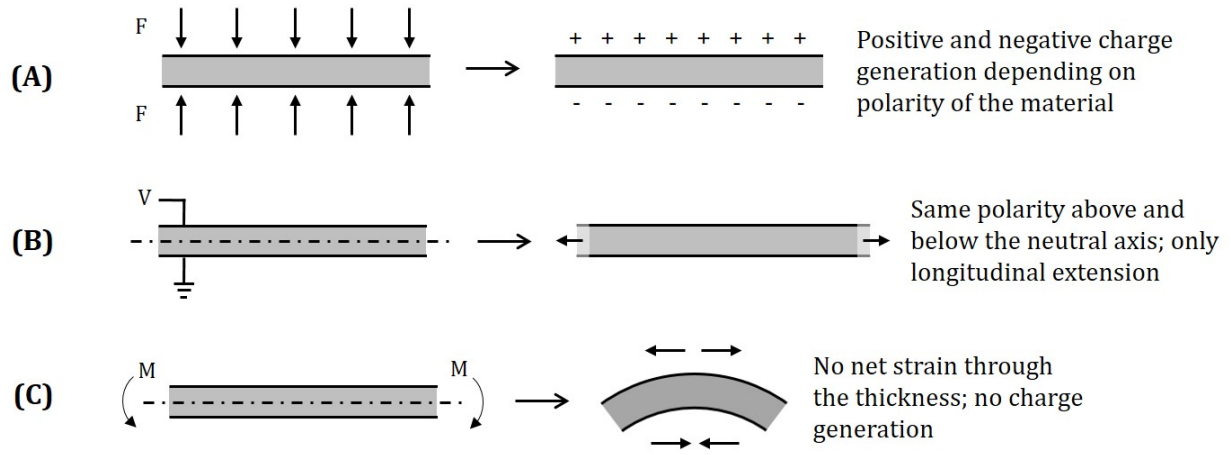

Figure 2.1: Schematic representations of the direct and inverse piezoelectric effect. Panel (A) illustrates an applied stress that results in charge generation on the electrodes of a piezoelectric element. Panel (B) shows the longitudinal extension that occurs when a voltage is applied to the electrodes and an electric field is generated within the material. Panel (C) demonstrates that a single piezoelectric element with an applied bending moment about its neutral axis will not generate any electrical signal due to a lack of net strain within the material.

Panel (B) illustrates the same beam with prescribed voltages applied to the electrodes (one is ground). The electric field generated thorough the layer thickness (in the 3-direction) causes a mechanical strain by the inverse piezoelectric effect. However, no effect is seen if the same beam is subjected to a pure bending moment, as shown in Fig. 2.1 panel (C). In that case, since the polarity of the material above and below the neutral axis is the same, the positive strain on through the top half of the element is equally opposed by the negative strain through the bottom half of the element and no charge is generated on the surface electrodes.

To successfully sense voltage from a bending piezoelectric element, or to achieve transverse deflection with a voltage input, it must be part of a layered structure [69, 70]. In other words, the neutral axis of the individual piezoelectric layer must lie above or below the neutral axis of all the layers combined. This can be achieved by including a structural layer with the piezoelectric layer (unimorph), or by using two or more stacked piezoelectric layers (bimorph or multimorph). A piezoelectric bimorph is demonstrated in Fig. 2.2; when a me-

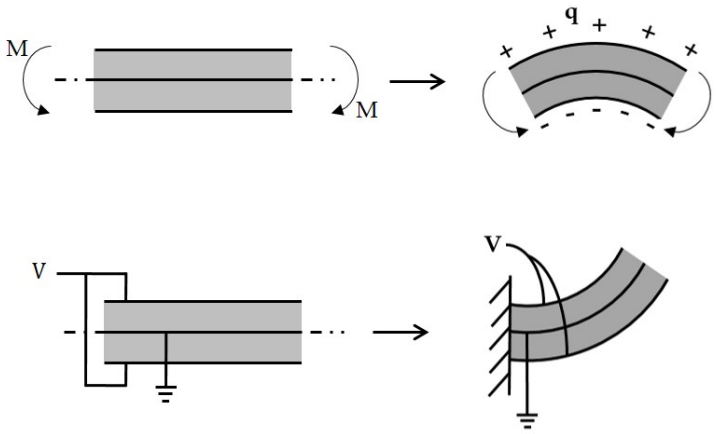

Figure 2.2: Schematic representations of the direct and inverse piezoelectric effect for a piezoelectric bimorph structure. At the top, the bimorph is subject to a bending moment about the combined neutral axis and results in charge accumulation due to all positive or all negative strain through the thickness of the layer. At the bottom, a voltage is applied to a bimorph (accounting for material polarity and extension direction) causing bending deflections of the layered beam.

chanical moment is applied, both layers are able to generate charge on their electrodes since they experience all positive or all negative strain through the full layer thickness. Similarly, a bimorph that is appropriately electrically connected (accounting for the material polarity) will deflect in response to applied voltage, which is the result of one layer expanding while the other layer contracts. Assuming the layers are identical, the longitudinal extension at the neutral axis will be cancelled and the beam will be in pure bending.

2.2.2 Connecting Piezoelectric Elements Electrically

Each individual piezoelectric layer in one of these beam structures can be represented electrically as a current source in parallel with the layer capacitance. As mentioned briefly in the preceding section, the choice of layer connection is important for both obtaining a voltage signal from a piezoelectric structure and actuating it with a voltage. In addition, it is also possible to connect independent beams to obtain a desired output. For any of these purposes, there are four possible connection combinations - series or parallel and in- or out-of-phase. These are represented in the chart in Fig. 2.3.

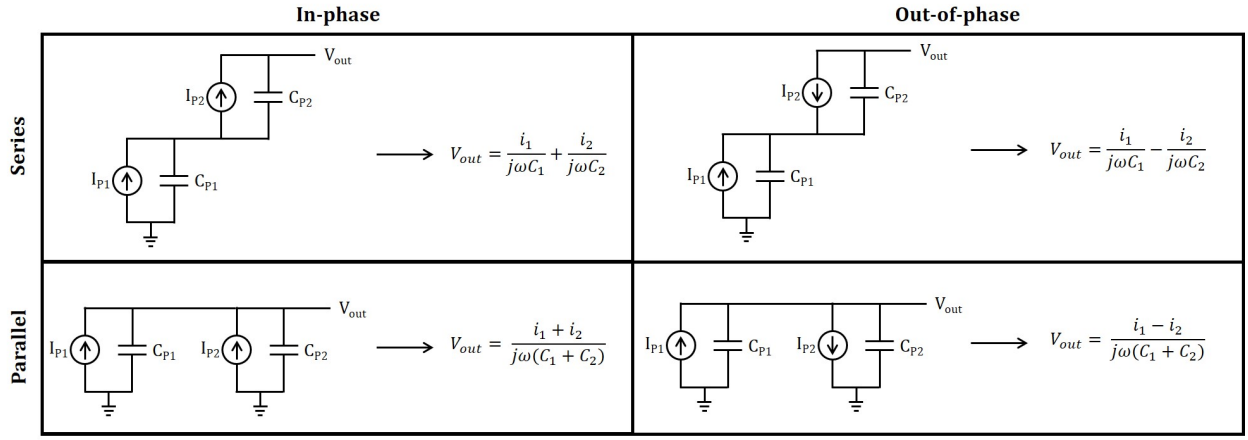

Figure 2.3: Circuit representations of series and parallel in- and out-of-phase connection combinations of piezoelectric elements. The series, in-phase combination is simply a sum of voltage outputs from the individual sensors, while the out-of-phase combination is a difference of the voltages. Similarly, the parallel, in-phase combination is a sum of the current generated by each sensor sent through the total impedance of the parallel capacitors. The out-of-phase result is a difference in currents through this same capacitive impedance. This chart includes examples of two connected elements, but any number is possible and will follow these equations.

As seen in the example circuits, the total voltage output from series-connected piezoelectric elements is a sum of the voltage outputs for in-phase connections and a difference for out-of-phase connections. For parallel-connected piezoelectric elements, the result is a sum or difference of the individual generated currents passed through the impedance of the parallel capacitors. It is important to properly account for the phase connection since an out-of-phase connection of identical elements will result in signal cancellation. Although these trends are demonstrated with two sensing elements for the sake of simplicity, any number of connected elements are possible. The concepts presented in this chart will become important for the sensor design described in Chapter IV.

2.2.3 Series and Parallel Resistor-Capacitor Representations of Impedance

Although the simple piezoelectric circuits in the previous section only included the ideal capacitance of the element, they actually have losses represented by a parallel or series

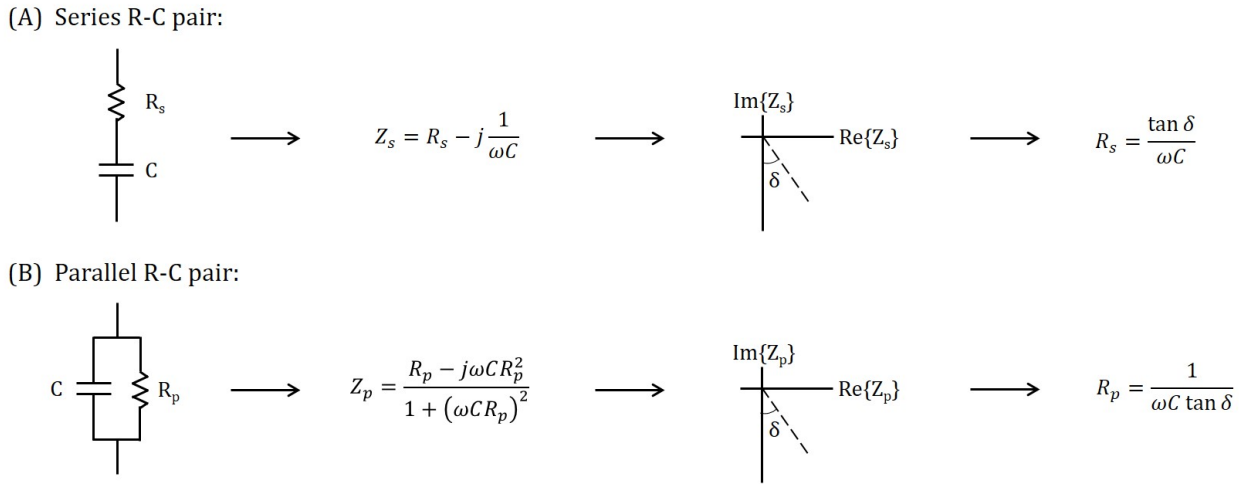

Figure 2.4: Series and parallel resistor-capacitor pair representations for the lossy capacitive sensing element. Panels (A) and (B) provide the impedance equation for each respective pair as well as the resistance value in terms of dissipation factor, tanδ.

equivalent resistance. These resistor-capacitor (R-C) pair options are presented in Fig. 2.4 along with the calculated series or parallel impedance, Z_s or Z_p, respectively. If the real and imaginary components of the impedance are plotted on orthogonal axes, the dielectric loss factor is the tangent of δ, the angle by which the imaginary part lags the real part. This parameter will be denoted as $\tan\delta$ throughout the remainder of this document. In either case, the capacitance value and $\tan\delta$ are the same, but the value of the resistor changes with each representation to maintain the same overall device impedance.

Conveniently, both representations have the same real part when the resistor value defined in terms of tanδ is substituted into the corresponding impedance expression. Therefore, the noise voltage generated by the dielectric material losses is the same regardless of the chosen R-C representation. However, the equivalent series or parallel resistance distinction is important for measuring this value experimentally, but does not play a large role in the system models.

2.3 Analytic Model of the Bimorph Accelerometer

2.3.1 Design Concept

The general acceleration sensor structure considered in this work is depicted in Fig. 2.5. It comprises a piezoelectric beam affixed to a rigid silicon (Si) frame at one end with a Si proof mass attached at the other end. The beam has length L defined in the x-direction and total thickness t_b defined in the z-direction. The bimorph beam is made of two active piezoelectric layers that are covered by electrode material starting at the base of the structure and extending to length L_e on the top and bottom surfaces and separated by a full-length electrode in the middle. In this system, the electrode length is constrained to the range $0 < L_e \leq L$.

The mass is assumed to be a rigid body of length L_M that sits flush with the top face of the beam and hangs downward as defined by its thickness, or height, t_M; it has mass M and mass moment of inertia I_M defined about the point where the mass meets the neutral axis of the beam (center electrode). The beam and the mass are designed to be the same width, b, in the y-direction (into the page). W_{bz} is the prescribed base displacement in the z-direction representing the vibration input to the sensor. In conjunction with W_{bz}, the

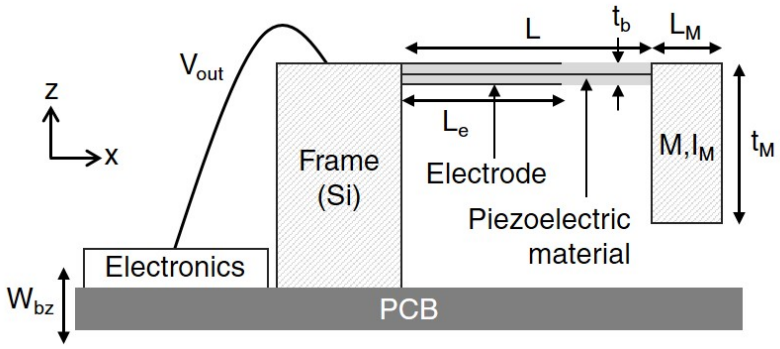

Figure 2.5: Diagram of the modeled structure. The device is a piezoelectric cantilever bimorph beam of length L made of AlN with a total thickness t_b. A silicon proof mass with dimensions L_M and t_M, mass M, and moment of inertia I_M is attached to the end of the beam. The beam is anchored to a silicon frame that sits on a PCB carrier that also includes the signal processing electronics for the voltage output V_{out}.

the physical connections to the frame and mass define the boundary conditions needed to determine the transverse motion of the beam and therefore its piezoelectric voltage output, V_{out}. The piezoelectric layers are electrically connected in parallel, and the voltage output is sent to electrical components on a printed circuit board (PCB) that condition the signal during experimental testing.

As opposed to constrained piezoelectric structures [71], the cantilevered configuration will release stresses developed during layer deposition, avoiding the need for detailed residual stress analysis. In this design, the location of the center of gravity of the proof mass is not ideal, but is designed to the realities of planar microfabrication processes. Since it lies below the neutral axis of the beam, the device will also be sensitive to motion in the x-direction. In the derivations that follow, we assume that there is no excitation in the x-direction and proceed to find the z-direction sensitivity solution. A brief explanation of the x-direction sensitivity solution is given in Appendix A.4.

2.3.2 Sensitivity

To design the accelerometer, we model its sensitivity, the frequency-dependent voltage output with respect to input acceleration in the z-direction. We assume Bernoulli-Euler beam hypotheses where plane sections remain plane and the strain in the x-direction is

$$\varepsilon_x = \frac{dU_0(x)}{dx} - z\frac{d^2W(x)}{dx^2} \ . \tag{2.3}$$

The longitudinal extension of the neutral axis of the beam, $U_0(x)$, and its derivative are assumed to be zero in this case. Considering harmonic time dependence, the transverse (bending) vibration of a beam, $W(x)$, is modeled by the following ordinary differential equation:

$$\overline{EI}\frac{d^4W(x)}{dx^4} - \omega^2\rho AW(x) = 0 \ . \tag{2.4}$$

Here, ω is frequency, ρ is the density of the piezoelectric material, and A is the cross-sectional area of the beam defined as $A = 2t_{piezo}b$ where b is the width of the beam and t_{piezo} is the thickness of a single piezoelectric material layer. $\overline{EI}$ in this equation is the beam bending stiffness that takes piezoelectricity into account. The full derivation of the piezoelectric bending stiffness can be found in Krommer and Littrell and Grosh [69, 70]. $\overline{EI}$ for the two-layer structure considered in this work is simply

$$\overline{EI} = \frac{bt_{piezo}^3}{s_{11}}\left(\frac{2}{3} + \frac{1}{6}\frac{d_{31}^2}{\epsilon_{33}}\right) . \tag{2.5}$$

In Eq. 2.5, d_{31} is the piezoelectric coefficient, s_{11} is the material's elastic compliance, and ϵ_{33} is its permittivity. Since the electrodes are thin layers, their effect on the beam bending mechanics is neglected. However, if the residual stress or the thickness of these electrode layers is non-negligible, then this effect can be included in the calculation of bending stiffness [69, 70].

The free vibration solution to the differential equation (Eq. 2.4) can be written in the form

$$W(x) = C_1 \sin(kx) + C_2 \cos(kx) + C_3 \sinh(kx) + C_4 \cosh(kx) \tag{2.6}$$

where the wave number is $k^4 = \rho A\omega^2/\overline{EI}$. The constants C_1 through C_4 are determined with the boundary conditions defined for the system. At the connection to the frame, $x = 0$, the boundary conditions include the prescribed base displacement in the z-direction

$$W(0) = W_{bz} \tag{2.7}$$

and the zero slope condition

$$\frac{dW(0)}{dx} = 0 . \tag{2.8}$$

The proof mass generates the following moment and force boundary conditions at $x = L$:

$$\overline{EI}\frac{d^2W(L)}{dx^2} = \frac{1}{2}ML_M\omega^2W(L) + I_M\omega^2\frac{dW(L)}{dx} + \overline{M_e} \tag{2.9}$$

$$\overline{EI}\frac{d^3W(L)}{dx^3} = -M\omega^2W(L) - \frac{1}{2}ML_M\omega^2\frac{dW(L)}{dx} \ . \tag{2.10}$$

The displacement-dependent term in Eq. 2.9 and the slope-dependent term in Eq. 2.10 result from the moment and force generated by the rigid body motion of the mass center of gravity that is far from the beam attachment location. $\overline{M_e}$ in Eq. 2.9 is the electrical moment contribution of the bimorph piezoelectric beam that has identical layers connected in parallel and is defined as

$$\overline{M_e} = -\frac{bd_{31}t_{piezo}}{s_{11}}V_P \ . \tag{2.11}$$

V_P is the potential difference across each of the piezoelectric layers that generates this electrical moment which opposes the mechanical moment condition (the derivation of this is also given in Krommer [69]). In the moment condition in Eq. 2.11, the electrode length is assumed to be equal to the full beam length, otherwise the electrical moment would be applied at L_e with a Dirac delta function.

The final expression needed to close this system of equations and solve for the sensitivity is the voltage output from the connected piezoelectric layers, V_P. To derive this expression, we return to the piezoelectric coupling equations which now have a reduced form not only from the material symmetry assumptions mentioned previously, but also according to the uniaxial stress constitutive hypothesis associated with Bernoulli-Euler theory [55, 30]. In this case, $\sigma_x \neq 0$ while $\sigma_y = \sigma_z = 0$ (note that the axis labels have been translated from 1, 2, and 3 to x, y, and z for the stress and strain of the modeled system, but the subscripts of the material properties remain in numeral form). Additionally, with electrodes defined on the top an bottom surfaces, only $E_3 \neq 0$. These assumptions result in the following form of

the coupling equations:

$$\varepsilon_x = s_{11}^E \sigma_x + d_{31} E_z \tag{2.12}$$

$$D_z = d_{31} \sigma_x + \epsilon_{33}^\sigma E_z \ . \tag{2.13}$$

To calculate the charge generated from each piezoelectric layer, first solve Eq. 2.12 for σ_x and substitute the result into Eq. 2.13. Next, insert Eq. 2.3 for ε_x. Finally, integrate the new D_z expression through the thickness (z-direction) to determine the total strain contribution and over the electrode area (x- and y-directions) to determine the total charge [69].

Two key assumptions are made during this process: first, the neutral axis of the beam lies at the location of the center electrode (owing to two piezoelectric layers with identical properties and dimensions); second, the center electrode is held at ground voltage. In a parallel connection, the charge output from the layered beam is $Q_p = Q_b - Q_t$ (Q_b is from the bottom layer and Q_t is from the top layer) and the electric potential on the top and bottom electrode will be equal. Therefore, the sensor equation for the bimorph is

$$Q_p = C_p V_p + \frac{d_{31} b t_{piezo}}{s_{11}} \frac{dW(L)}{dx} \tag{2.14}$$

where $C_p = 2\hat{\epsilon}_{33} bL/t_{piezo}$ is the parallel capacitance of the beam layers and $\hat{\epsilon}_{33} = \epsilon_{33} - d_{31}^2/s_{11}$.

To determine the open circuit sensitivity of this device design ($Q_p = 0$), we assemble the boundary conditions and the electrical equation (Eq. 2.14) in a matrix of terms associated with each coefficient (C_1-C_4) and V_p. The matrix equation is the following:

$$\begin{bmatrix} 0 & 1 & 0 & 1 & 0 \\ k & 0 & k & 0 & 0 \\ X_1 & X_2 & X_3 & X_4 & \alpha \\ X_5 & X_6 & X_7 & X_8 & 0 \\ \alpha k \cos(kL) & -\alpha k \sin(kL) & \alpha k \sinh(kL) & \alpha k \cosh(kL) & C_p \end{bmatrix} \begin{bmatrix} C_1 \\ C_2 \\ C_3 \\ C_4 \\ V_p \end{bmatrix} = \begin{bmatrix} W_{bz} \\ 0 \\ 0 \\ 0 \\ 0 \end{bmatrix} \tag{2.15}$$

where $\alpha = d_{31} b t_{piezo} / s_{11}$. The expressions for X_1-X_8 are given in Appendix A.1 for the interested reader. Any value of W_{bz} can be chosen to solve this system of equations, but $W_{bz} = 1$ is a convenient solution to determine the normalized voltage output V_p to the base displacement input. The conversion to acceleration sensitivity in the z-direction, $S_Z = V_p / \ddot{W}_{bz}$, is simple for harmonic forcing where $\ddot{W}_{bz} = -\omega^2 W_{bz}$. The resulting units are V/(m/s^2) or V/g.

2.3.3 Actuation

Piezoelectric actuator design has much different application-specific requirements compared to sensor design. Even so, the sensors will be actuated during experimental testing to verify their functionality and to measure material properties [70]. A simple model can be derived from the equations already developed for sensing.

$$\begin{bmatrix} 0 & 1 & 0 & 1 \\ k & 0 & k & 0 \\ -X_1/\alpha & -X_2/\alpha & -X_3/\alpha & -X_4/\alpha \\ X_5 & X_6 & X_7 & X_8 \end{bmatrix} \begin{bmatrix} C_1 \\ C_2 \\ C_3 \\ C_4 \end{bmatrix} = \begin{bmatrix} 0 \\ 0 \\ V_p \\ 0 \end{bmatrix} . \tag{2.16}$$

α is calculated as before, and setting $V_p = 1$ will result in a beam deflection results that are normalized to voltage. Using Eq. 2.6, displacement, velocity, and acceleration, as well as slope, moment, and force can be determined for any point along the length of the beam. As will be discussed in Chapter III, the velocity at $x = L$ is the measured quantity for actuation experiments, which is converted to acceleration with a factor of $j\omega$ and presented in units of m/s^2/V.

2.3.4 Noise

Next, we need an expression for the output electrical-thermal noise spectral density expected from intrinsic dielectric losses of the piezoelectric material [72]. The thermal fluc-

tuations in the material generate a small voltage that can be calculated using the familiar Johnson noise equation

$$\overline{v_n^2} = 4k_B T|Re(Z)|\delta f \tag{2.17}$$

where k_B is the Boltzmann constant, T is temperature in Kelvin, $Re(Z)$ is the real part of the electrical impedance of the piezoelectric layer (as mentioned in Section 2.2.3), and δf is the frequency bandwidth. We represent the piezoelectric layer as a parallel R-C pair and connect two of them in parallel to define the impedance Z, which includes the relationship between the resistance and the dielectric loss of the material, $\tan\delta$, discussed previously [30, 55]. The resulting voltage noise expression, reported in units of V^2/Hz, is

$$\frac{\overline{v_n^2}}{\delta f} = \frac{4k_B T \tan\delta}{\omega C_P} \ . \tag{2.18}$$

This expression also depends on the chosen piezoelectric material and dimensions of the beam through the calculation of capacitance.

2.3.5 Minimum Detectable Acceleration

The minimum detectable acceleration (MDA) of the system represents the lowest detectable signal of the sensor, and as such it is the most important design criteria for a low-amplitude vibration sensing applications. By designing to this parameter, it is possible to ensure that the sensor can detect a certain input signal level at a particular frequency or over a range of frequencies. MDA is defined as

$$MDA_Z = \frac{\sqrt{\overline{v_n^2}}}{S_Z} \quad , \tag{2.19}$$

where S_Z is the previously determined z-direction sensitivity of the system and $\overline{v_n^2}$ is the spectral density in 1 Hz bandwidths. For clarity, the subscript "z" for MDA denotes that S_Z is used. For a sensitivity expressed as $V/(m/s^2)$ or V/g, the MDA is expressed in units

of $(\mathrm{m/s^2})/\sqrt{\mathrm{Hz}}$ or $\mathrm{g}/\sqrt{\mathrm{Hz}}$, respectively, for these sensors.

2.4 Assumed-mode Analytic Model

2.4.1 Sensitivity, Noise, and Minimum Detectable Acceleration

The solution obtained in the section above does not readily allow for the observation of trends in S_Z with varying parameters such as beam or mass dimensions. Therefore, an assumed mode solution is used to obtain an estimate of S_Z, denoted $\tilde{S}_Z$, and assess the low-frequency behavior of this system in response to parameter changes. The chosen mode shape is that of a statically bending beam with a transverse displacement described by the following cubic equation

$$\tilde{W}(x) = \tilde{C}_1 x^3 + \tilde{C}_2 x^2 + \tilde{C}_3 x + \tilde{C}_4 \; . \tag{2.20}$$

Using the boundary conditions Eqs. 2.7-2.10 and the sensing equation Eq. 2.14 we arrange the matrix equation to solve for the coefficients $\tilde{C}_1$-$\tilde{C}_4$ and V_p for the particular solution as follows

$$\begin{bmatrix} 0 & 0 & 0 & 1 & 0 \\ 0 & 0 & 1 & 0 & 0 \\ \tilde{X}_1 & \tilde{X}_2 & \tilde{X}_3 & \tilde{X}_4 & \alpha \\ \tilde{X}_5 & \tilde{X}_6 & \tilde{X}_7 & \tilde{X}_8 & 0 \\ 3\alpha L^2 & 2\alpha L & \alpha & 0 & C_p \end{bmatrix} \begin{bmatrix} \tilde{C}_1 \\ \tilde{C}_2 \\ \tilde{C}_3 \\ \tilde{C}_4 \\ V_p \end{bmatrix} = \begin{bmatrix} W_{bz} \\ 0 \\ 0 \\ 0 \\ 0 \end{bmatrix} \; . \tag{2.21}$$

The expressions for $\tilde{X}_1$-$\tilde{X}_8$ are given in Appendix A.2. Again, the acceleration sensitivity is found by multiplying the normalized voltage output with respect to base displacement (when $W_{bz} = 1$) by a factor of $-1/\omega^2$.

Due to the dynamic boundary conditions, the resulting sensitivity equation is still frequency dependent. To analyze the low-frequency behavior of the system, we take the limit of this equation as frequency ω goes to zero. The result is a closed-form solution for the

low-frequency asymptote of the voltage sensitivity equation

$$\tilde{S}_Z = -\frac{3}{2}\frac{d_{31}Ms_{11}}{bt_{piezo}}\frac{(L+L_M)}{(3d_{31}^2 - 4\epsilon_{33}s_{11})} \tag{2.22}$$

which clearly illustrates the sensitivity dependence on material properties and the physical dimensions of the beam and mass. Finally, inserting Eqs. 2.22 and 2.18 into Eq. 2.19 above ($\tilde{S}_Z$ replacing S_Z in that expression) yields the low-frequency MDA for the assumed-mode solution

$$MDA_Z = \sqrt{\frac{8k_BT}{9}}\frac{1}{\sqrt{\omega}}\frac{(3d_{31}^2 - 4\epsilon_{33}s_{11})\sqrt{\tan\delta}}{d_{31}s_{11}\rho_{mass}\sqrt{\epsilon_{33}}}\frac{\sqrt{t_{piezo}^3}}{L_M t_M\sqrt{bL}(L+L_M)}\ . \tag{2.23}$$

This closed-form MDA expression is written here in a form with four distinct groups of parameters. The first group is a set of constants since k_B is known and T is defined based on the expected environmental temperature of the sensor during use (in units of Kelvin). Next, the expression retains the frequency dependence from the noise generated by the piezoelectric material in the factor $1/\sqrt{\omega}$. Then the material properties are grouped, which come from both the sensitivity and the noise calculations discussed above. The only parameter that is not associated with the piezoelectric material is the density of the mass material, ρ_{mass}. Finally, the physical dimensions of the beam and mass are grouped; they are the most important parameters in this design equation. Once the piezoelectric and substrate materials are chosen, their properties are defined and not variable for optimization. Conversely, all of the dimensions, or a chosen subset of them, can be varied to determine the combination that provides the smallest MDA possible within given value ranges that are sensible for fabrication capabilities or size constraints. Examples using the MDA expression will be given in Section 2.4.3.

2.4.2 Resonant Frequency Approximation

As seen in Eq. 2.23 above, increasing the beam and mass lengths will decrease the resulting MDA. Sensor designs optimized with only this equation will have low resonant frequencies as a direct result of increasing these dimensions. However, the resonant frequency dictates the operating bandwidth of the sensor that is typically defined over the range of frequencies where the sensitivity is constant prior to the first resonance. Terminology such as "1 dB bandwidth" and "3 dB bandwidth" are common for commercial device specifications. For example, "3 dB bandwidth" means that the upper limit of the range is the frequency at which the sensitivity increases to 3 dB above the constant low-frequency value (often chosen at 100 Hz). While using the MDA expression as a design tool, it is imperative to include resonant frequency checks in the process to ensure that bandwidth requirements are also achieved.

The resonant frequency of this system can be found with the solution to the differential equation given in Section 2.3.2 with homogeneous boundary conditions. As was true with the forced solution, the result retains frequency dependence in the wave number within hyperbolic and regular trigonometric functions. Conveniently, the assumed-mode case presented in this section can be used to estimate the resonant frequency of the system without needing a Taylor series expansion and simplification of all frequency-dependent terms. Following from the preceding matrix equation (Eq. 2.21), a simplified 2x2 matrix results for homogeneous boundary conditions where $C_3 = 0$ by Eq. 2.8, $C_4 = 0$ by Eq. 2.7 when $W_{bz} = 0$, and the voltage term in Eq. 2.9 is replaced with Eq. 2.14 when $Q_p = 0$. The terms are assembled in the following matrix

$$\det \begin{bmatrix} 3L(2\overline{EI} - \frac{\alpha^2}{C_p}L) - (\frac{1}{2}ML_ML + 3I_M)L^2\omega^2 & 2(\overline{EI} - \frac{\alpha^2}{C_p}L) - (\frac{1}{2}ML_ML + 2I_M)L\omega^2 \\ 6\overline{EI} + ML^2\omega^2(L + \frac{3}{2}L_M) & -ML\omega^2(L + L_M) \end{bmatrix} = 0 \tag{2.24}$$

of which the determinant is taken, resulting in a quadratic equation for ω^2, $\tilde{A}(\omega^2)^2 + \tilde{B}(\omega^2) +$

$\tilde{C} = 0$, after simplifying and grouping terms. The coefficients $\tilde{A}$, $\tilde{B}$, and $\tilde{C}$ are given for reference in Appendix A.3. The quadratic formula can be used to find solutions ω_1^2 and ω_2^2 which are the squares of the first and second resonant frequencies of the system. With ω_1 known for each combination of dimension parameters, a limit can be set to ensure that the bandwidth remains sufficiently large. This will be exemplified more specifically for the case study in the following section.

2.4.3 Case Studies using MDA Design Equation

In this section, we present two case studies to demonstrate the use of the MDA design equation derived in Section 2.4.1. Each study will demonstrate a different approach. First, with some parameters defined by material choice and fabrication process norms or limitations, we will find the minimum MDA of dimension combinations that meet a particular resonant frequency specification. Second, we will seek the sensor width b necessary to achieve a particular MDA for a given set of dimensions. Both of these approaches rely on the fact that increasing b monotonically decreases the MDA without affecting the resonant frequency of the sensor (since the beam width and mass width are assumed to be identical) so it can be defined independently. The width does, however, directly affect the overall sensor size; as will be demonstrated with the second design approach, for certain dimension combinations the width must be significantly large to achieve the desired MDA. If the sensor size exceeds reasonable limitations set for the application, then the overall set of parameters for the design is not feasible.

2.4.3.1 Approach 1: Minimum MDA

To begin, we reduce the number of variables in the design equation by choosing a test frequency for the calculation and specifying materials for the piezoelectric beam and proof mass volume. In this example, we use aluminum nitride (AlN) material properties and assume, as stated in Section 2.3.1, that the mass is made of silicon. The properties of

these materials will not affect the MDA trends investigated in this approach. Hence, the specific values for the compliance, piezoelectric coefficient, relative permittivity, loss tangent, and silicon density will not be given in this section (see Chapter III for this information). However, the beam properties do affect the resonant frequency so the material definitions are necessary to accurately assess the resonant frequency of each dimension combination. The test frequency (for the $1/\sqrt{\omega}$ term) in this example is 100 Hz since the MDA increases with decreasing frequency. In other words, the lower limit of the desired bandwidth will have the highest MDA.

In this process, it is also helpful to eliminate some of the dimension variables from the optimization problem. Since b can be independently defined for any design, we choose 100 µm in this calculation. Additionally, the piezoelectric material thickness is often dictated by microfabrication processes used to deposit high-quality films of the material. For AlN, a common and reliably high-quality layer thickness is 0.5 µm [55, 67]. With these choices made, the remaining variables to consider in this approach are L, L_M, and t_M. For reference, this subset of variables from the MDA expression follows the relationship

$$MDA_{sub} = \frac{1}{L_M t_M \sqrt{L}(L + L_M)} \ . \tag{2.25}$$

For this approach, we study pseudo-color plots of L and L_M combinations for chosen values of t_M to find the combination with the lowest MDA for each mass thickness, then choose the lowest MDA from those options. With current microfabrication processes, the resolution of the surface dimensions (i.e. the x-y planar dimensions) can be more easily controlled than the thickness (z-direction) dimensions; hence, fewer mass thicknesses are considered in this analysis.

Before assessing the length combination results for various thicknesses, we examine how the increment resolution of the length dimensions affects this procedure. This choice, in general, is predicated upon the fabrication processes having the same or finer resolution

capabilities than the chosen length discretization. Figure 2.6 shows the MDA results for L and L_M ranging from 50-300 µm; in Runs 1 and 2, the lengths were divided into 25 µm and 10 µm increments, respectively. The mass thickness in both runs is 500 µm. The MDA color is scaled logarithmically over the same range of values for both plots, and the contour line on each plot indicates the 600 Hz resonant frequency limit. Dimension combinations above this line (top-right of the plot) have a resonant frequency below 600 Hz since the beam and mass both get longer. Below the contour (bottom-left of the plot), the dimension combinations result in resonant frequencies greater than 600 Hz.

On the plot for each resolution run, a black star marks the dimension combination with the lowest MDA that also has a resonant frequency above the chosen 600 Hz limit. For Run 1, L = 50 µm and L_M = 275 µm, MDA_Z = 8.4x10^{-5} m/s^2/$\sqrt{\text{Hz}}$ and the resonant frequency is 625.7 Hz. Run 2 also results in L = 50 µm, but L_M = 290 µm; MDA_Z = 7.6x10^{-5} m/s^2/$\sqrt{\text{Hz}}$ and the resonance is 601 Hz. As another example, the black circle on each plot indicates the equal-length combination that is closest to the resonant frequency line. The $L = L_M$ = 125 µm combination has a resonant frequency of 814 Hz, which decreases to 662 Hz for $L = L_M$ = 130 µm. The MDA also decreases from 2.7x10^{-4}

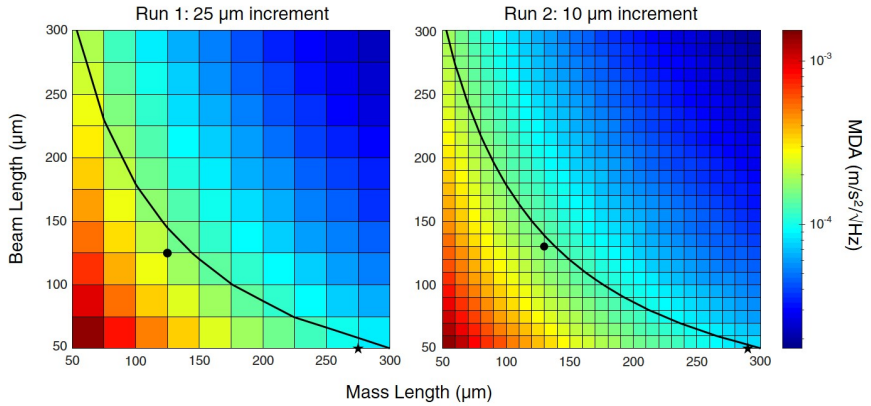

Figure 2.6: MDA pseudo-color plots for length combinations discretized into 25 µm and 10 µm increments with a mass thickness of 500 µm. The contour line indicates the resonant frequency of 600 Hz. The black star on each plot marks the lowest MDA combination, and the black circle indicates the equal-length combination. Results indicate that the finer resolution improves the MDA result by achieving a resonant frequency closer to the set limit.

to 1.7x10^{-4} m/s^2/$\sqrt{\text{Hz}}$. Ultimately, it is shown that the finer mesh resolution for length combinations improves the MDA by increasing the likelihood that the resonant frequency lies close to the contour line indicating the desired limit. It is important to remember that there are limitations to fabrication resolution, particularly with reactive ion etching (RIE) processes, so it may not be possible to specify dimensions much smaller than what we have demonstrated here. Hence, we proceed with this approach considering 10 µm increment for the beam and mass lengths.

The tested length range for the mass thickness comparisons is still 50-300 µm. The 50 µm lower limit is chosen to maintain conservative aspect ratios for fabrication (specifically referring to etching between the vertical side walls of the frame and proof mass). In this demonstration, we calculate the MDA for L and L_M for five different t_M values (100-500 µm in 100 µm increments). A resonant frequency limit of 1 kHz is chosen for this example. The MDA results for each thickness are provided in the five plots in Fig. 2.7, starting with t_M = 500 µm and decreasing to t_M = 100 µm. Representative colors are identically scaled for each plot, ranging from the lowest MDA in the t_M = 500 µm case (darkest blue) to the highest MDA in the t_M = 100 µm case (darkest red). As expected, the number of combinations above the resonant frequency limit increases with decreasing mass thickness; this is seen as the frequency line shifts to the upper-right corner of the plot. It is also clear that combinations with higher resonant frequencies also have high MDA values, attributed to the decrease in sensitivity.

The best MDA result for each mass thickness is marked with a black arrow on each respective plot; all of the combinations, MDA values, and resonant frequencies (denoted f_R) are consolidated in Table 2.1. Of these five MDAs, the best result comes from the t_M = 300 µm case when L = 50 µm and L_M = 300 µm. This combination has a resonant frequency of 1009 Hz and the $MDA_Z = 1.2x10^{-4}$ m/s^2/$\sqrt{\text{Hz}}$. In this example, the upper limit of the mass length affects the final result. When the resonant frequency line intersects the mass length axis (i.e. some mass lengths decrease the resonance below the limit), the minimum

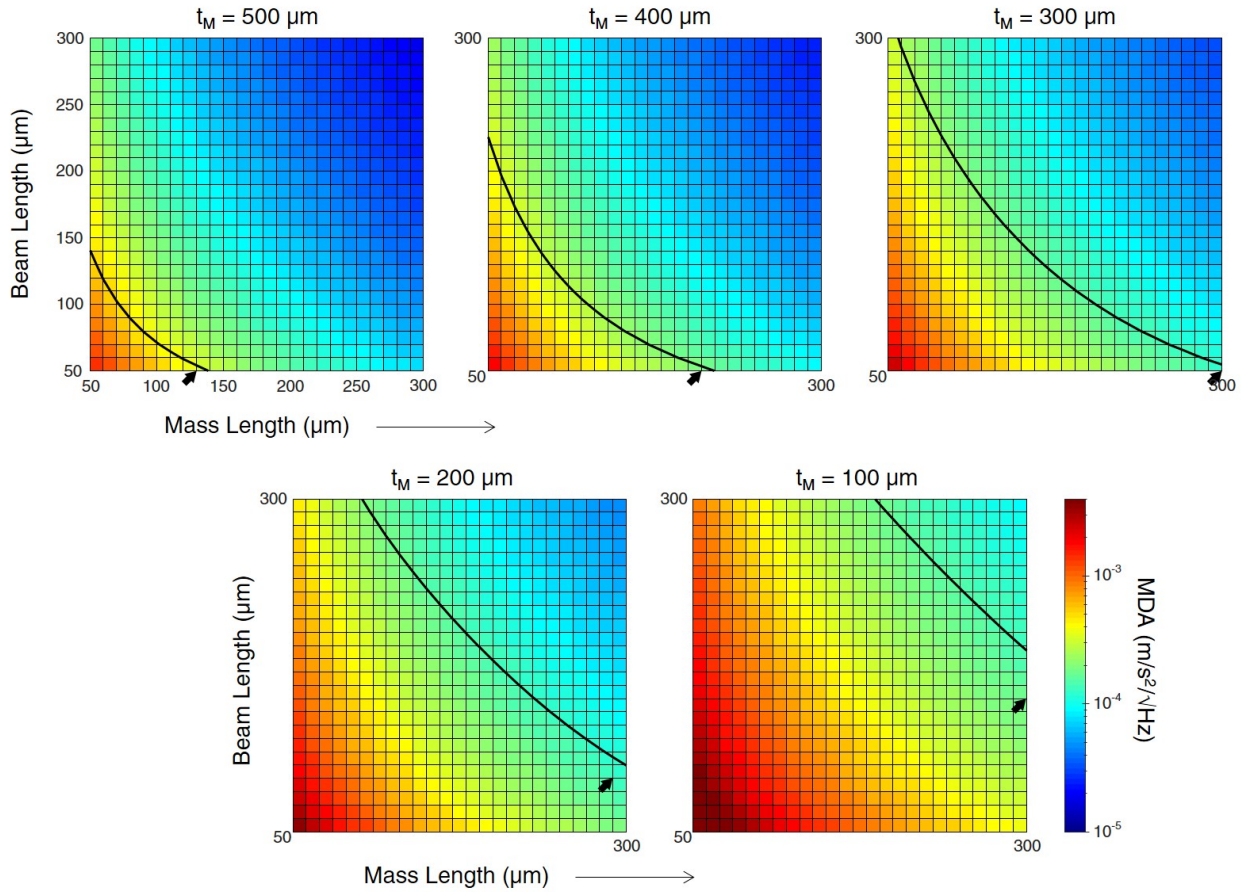

Figure 2.7: Length combination MDA results for five different mass thicknesses. Masses from 500 µm thick down to 100 µm thick are plotted over the same MDA range. The resonant frequency contour reference is 1 kHz. Decreasing the mass thickness results in combinations with higher resonant frequencies, but also higher MDA values. The black arrow on each plot marks the combination with the lowest MDA in each case.

Table 2.1: MDA and resonant frequency (f_R) for best dimension combinations

t_M (µm)	500	400	300	200	100
L (µm)	50	50	50	90	150
L_M (µm)	130	210	300	290	300
MDA ($m/s^2/\sqrt{Hz}$)	$3.2x10^{-4}$	$1.7x10^{-4}$	$1.2x10^{-4}$	$1.3x10^{-4}$	$1.6x10^{-4}$
f_R (Hz)	1014.5	1002.9	1008.9	1025.9	1049.7

MDA combination will always be the shortest beam length and the longest possible mass. However, when the mass length can no longer be increased, then the beam length will be increased to continue to lower the MDA and resonant frequency. These trends correspond to

the L_M^2 power compared to the $L^{3/2}$ power in the denominator of Eq. 2.25. If the mass length limit were increased for the 200 µm and 100 µm thick cases, better MDA results would be found with a shorter beam and a longer mass.

This case study, while not specific to any application, demonstrates one of the primary benefits of this closed-form MDA solution. That is, many dimension combinations (especially additional possibilities outside of application constraints) can be tested quickly during the sensor design phase without requiring 3-dimensional finite element solutions. This approach will be used to design the sensor discussed in Chapter IV.

2.4.3.2 Approach 2: b Control of MDA

To demonstrate the second approach to using the MDA expression for sensor design, we extrapolate from the previous approach with the set of dimensions that indicated the best MDA. For L = 50 µm, L_M = 300 µm, and t_M = 300 µm with the chosen test width b = 100 µm, the resonant frequency is 1009 Hz and the $MDA_Z = 1.2\text{x}10^{-4}$ m/s$^2/\sqrt{\text{Hz}}$. From the MDA expression given in Eq. 2.23, the $1/\sqrt{b}$ dependence is known; for convenience and visualization, the MDA results for sample values of b are plotted in Fig. 2.8. Consider, for instance, that $1.2\text{x}10^{-4}$ m/s$^2/\sqrt{\text{Hz}}$ found from the procedure in Approach 1 (red dotted line through this values) is 10 times too large for the target application. To decrease the MDA to

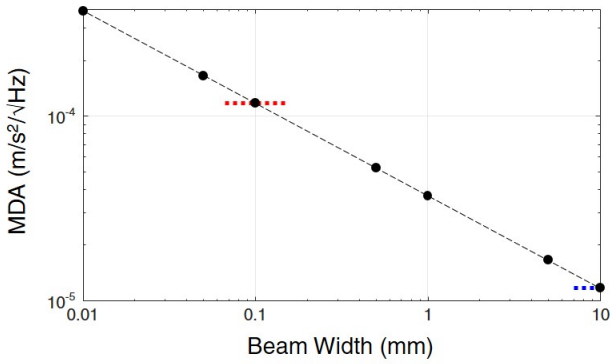

Figure 2.8: MDA dependence on beam width, b. Sample calculated values are marked with black circles, and the dashed line through them is the known $1/\sqrt{b}$ trend. A red dotted line highlights the MDA for the beam width used in Approach 1 (100 µm), and a blue dotted line indicates the desired MDA value (10x less) that results in a 10 mm wide beam.

the appropriate value, the beam width should be increased by 100 times, yielding a 10 mm wide beam (blue dotted line through this value). Based on MEMS die design experience, this beam could reasonably fit within an approximate die footprint less than 2 mm x 3 mm in area. This is achieved by dividing the total width into narrower segments and connecting the beams in parallel. The sensor size in this example is reasonable, but it may already be too large for some implantable biomedical applications (such as middle ear implantation). While this discussion only included hypothetical results and size limitations, it will be revisited for the realistic constraints of the middle ear accelerometer in the next chapter.

2.5 Model Validation with Finite Element Analysis

As seen in the case study above, the sensor design process for this configuration and application requirements will often result in wide beam structures (where $b > L$). This raises the question: is the uniaxial stress assumption associated with Bernoulli-Euler beam theory valid in this case? As the width increases, a plane-strain constitutive hypothesis may more accurately describe the transverse deflection and voltage output of this system [73]. In this section, we briefly derive the effective material constants associated with the plane-strain case and compare the analytical results to a finite element solution for the simple voltage actuation case.

Compared to a uniaxial stress state, for a plane-strain hypothesis we assume that σ_x and σ_y are non-zero, but $\sigma_z = \varepsilon_z = 0$ as before, as do all of the shear stress and strain components. Again, the electrical fields in the x and y-directions zero since those faces do not have electrodes, and the electric displacement is therefore also zero ($D_x = D_y = 0$).

These definitions lead to the following set of coupling equations:

$$\varepsilon_x = s_{11}^E \sigma_x + s_{12}^E \sigma_y + d_{31} E_z \tag{2.26}$$

$$\varepsilon_y = s_{21}^E \sigma_x + s_{22}^E \sigma_y + d_{32} E_z \tag{2.27}$$

$$D_z = d_{31} \sigma_x + d_{32} \sigma_y + \epsilon_{33}^\sigma E_z \ . \tag{2.28}$$

As before, indices are translated for the stress, strain, and electric field directions, but not for the material constant matrices. When the beam width increases, we consider $\varepsilon_y = 0$, solve Eq. 2.27 for σ_y, and insert that result into Eqs. 2.26 and 2.28. Based on the material symmetry considered here, $s_{11} = s_{22}$, $s_{12} = s_{21}$, and $d_{31} = d_{32}$. The new piezoelectric coupling equations take the same form as the previously discussed versions, but they have equivalents for the elastic compliance, piezoelectric constant, and permittivity. They are the following

$$\varepsilon_x = \tilde{s}_{11} \sigma_x + \tilde{d}_{31} E_z \tag{2.29}$$

$$D_z = \tilde{d}_{31} \sigma_x + \tilde{\epsilon}_{33} E_z \tag{2.30}$$

where $\tilde{s}_{11} = s_{11}(1 - s_{12}^2/s_{11}^2)$, $\tilde{d}_{31} = d_{31}(1 - s_{12}/s_{11})$, and $\tilde{\epsilon}_{33} = \epsilon_{33} - d_{31}^2/s_{11}$.

The analytic model presented in Section 2.3.3 is used to calculate the beam deflection at $x = L$, $W(L)$, for a sensor with $L = 100$ µm, $L_M = 50$ µm, and $t_M = 400$ µm. It is first solved with the uniaxial stress material constants, then the plane-strain constitutive hypothesis material constants. A 3-dimensional, piezoelectric, structural mechanics model is constructed in COMSOL Multiphysics software. Six beam widths are tested, including 10, 50, 100, 200, 400, and 800 µm. The results for $W(L)$ (at 100 Hz) and resonant frequency, f_R, are presented in Fig. 2.9A and Fig. 2.9B, respectively. In each plot, the red dashed line indicates the value for the plane-strain hypothesis and the blue dashed line is the value for the uniaxial stress assumption. They are plotted as lines since the modeled result does not

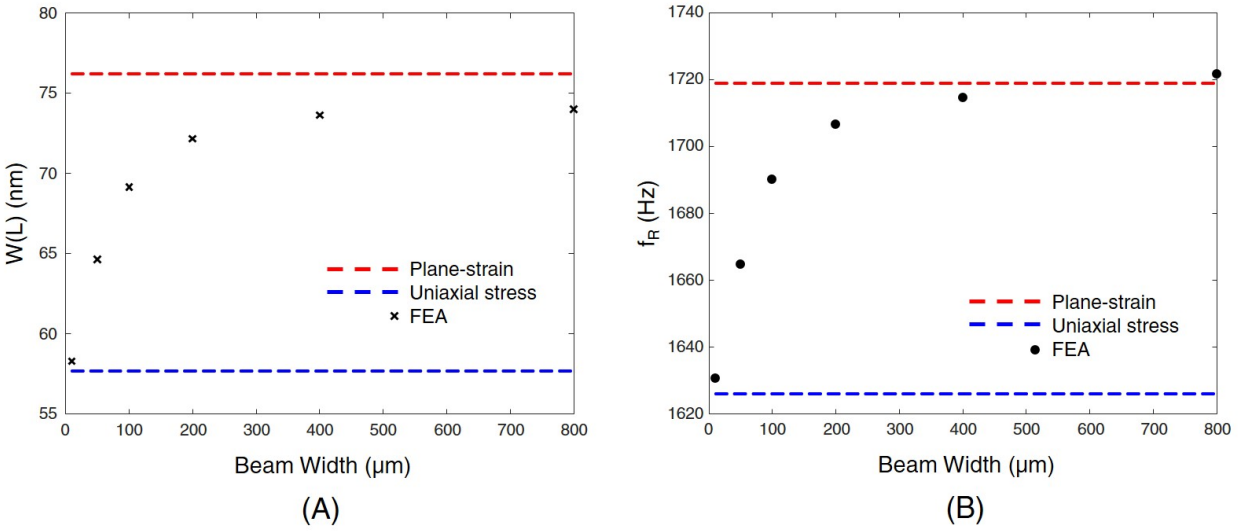

Figure 2.9: (A) Beam deflection $W(L)$ and (B) resonant frequency f_R results for increasing beam width. In both plots, the blue dashed line denotes the analytic uniaxial stress model, and the red dashed line denotes the analytic plane-strain model. Finite element solutions for $W(L)$ at the tested widths are marked with black "$\times$" symbols and the f_R solutions are marked with black circles. Beam deflection and resonant frequency simultaneously increase to the plane-strain asymptote.

change with increasing beam width. The black "$\times$" marks and black circles are the finite element analysis solutions at the tested beam widths.

The results demonstrate, as expected, that the resonant frequency increases due to the increased stiffness (decreased compliance) of the beam with the plane-strain assumption. Interestingly, $W(L)$ also increases, despite the increase in beam stiffness (in the uniaxial case, stiffer indicates less deflection). This is a result of the increased effective piezoelectric coefficient ($\tilde{d}_{31} > d_{31}$) since s_{12} is negative-valued and less than s_{11}, in conjunction with an increase in α calculated with $\tilde{d}_{31}$ and $\tilde{s}_{11}$. These results indicate that for beam length-to-width ratios greater than about 1:1, the plane-strain constitutive hypothesis provides a more accurate prediction of the beam response. However, fine-tuning of the design to ensure sufficiently high sensitivity or low enough noise floor should be completed with a full 3-dimensional finite element model of the sensor after analytic modeling is complete.

2.6 Conclusion

The aim of this chapter was to establish a model for the key design parameter of the MEMS piezoelectric accelerometer - its minimum detectable acceleration. MDA is highlighted as the key design variable because increasing sensitivity alone does not guarantee the ability to sense low-level inputs; the electrical noise floor of the sensor plays a large role in dictating the capabilities of the piezoelectric device. Full analytic models for the sensitivity, actuation response, and the MDA spectrum are presented. Additionally, low-frequency assumed mode solutions are provided that yield a design equation for the MDA. Two case study approaches to using this design equation are provided in a non-application-specific context.

The MDA expression indicates that increasing the sensor width for any set of design parameters will monotonically decrease the MDA. As such, it is found that the piezoelectric beams should be much wider than is valid for the original assumptions. Therefore, a comparison between the originally-assumed uniaxial stress state and a plane-strain hypothesis is completed, utilizing a finite element model solution for validation. It is shown that the wider structures are more accurately modeled with the plane-strain hypothesis, however, the design equation remains the same regardless of the hypothesis used. Advantageously, it can be used to quickly assess the design space without requiring lengthy finite element simulations.

CHAPTER III

First-generation Piezoelectric MEMS Accelerometer

This chapter discusses the model-validation experiments conducted with first-generation fabricated devices. The experimental procedures used to characterize important piezoelectric material properties and sensor performance are described in detail. The original model used here was the uniaxial stress assumption discussed in the previous chapter. During fabrication, we chose to fabricate stress-relief slits across the width of the beam, resulting in effectively 100 µm wide beam segments. This aspect ratio (1:1) falls between the two limiting constitutive hypothesis cases. Independent fitting of the piezoelectric coefficient with idealized structures (long, narrow beams) will be necessary for future iterations of device fabrication. Sections of this chapter have been previously published [74].

3.1 Accelerometer Design and Fabrication Process

First-generation devices were fabricated by collaborators at Vesper Technologies, Inc. using their proprietary process. This process and the available die space placed some restrictions on the physical sensor design variables. For instance, we knew that the sensor would be made of two layers of AlN, each 0.5 µm thick. Also, the height (thickness) of the proof mass was set at the wafer thickness of 400 µm since there were no process steps included to decrease this dimension. Therefore, the three remaining design variables were beam length (L), mass length (L_M), and beam and mass width (b, assumed to be the same, as stated in

the model description) for the first-generation sensors. As was also discussed in Chapter II, wider beams will help decrease the minimum detectable acceleration (MDA); however, the width was limited by the available die size in this case. Rather than use the MDA cost function to optimize the length dimensions for this design with respect to a particular resonant frequency limit, we chose conservative fabrication values to ensure sufficient yield of sensors from the processed wafer. The properties of Si and AlN necessary to model the accelerometer are listed in Table 3.1.

Two combinations of beam and mass parameters were fabricated, designated Design 1 and Design 2. Within each die, two of the structures were designed to be as wide as possible. Then, to effectively utilize the allotted die area, two narrower beams were placed on the remaining two internal edges of the frame. Top-down photographs of the fabricated MEMS die are shown in Fig. 3.1A. Design 1 has a beam length of 125 µm and a mass length of 75 µm, with beam widths of 700 µm and 300 µm. Design 2 has a 100 µm long beam and a 50 µm long mass, and has 700 µm and 400 µm widths. We also chose to include small (2 µm) etched slits every 100 µm across the beam width to decrease the effects of layer-deposition residual stress on the sensor performance. Each of the four beams has independent electrical connections and can be tested individually. The following sections in this chapter discuss the experimental testing of a 100 µm long, 700 µm wide beam, specifically pictured in Fig. 3.1B. As can be inferred from the photograph, this beam and proof mass were completely released from the frame of the die and the other proof masses after etching. In addition, the beam was visibly intact and preliminary measurements of the capacitance and dissipation factor (described in subsequent sections) indicated good AlN film quality.

Table 3.1: Material parameters for Si and AlN

	Si	AlN
ρ (kg/m^3)	2330	3260
s_{11} (m^2/N)	5.88x10^{-12}	2.9x10^{-12}
d_{31} (C/N)	–	-2x10^{-12}
ϵ_{33} (F/m)	–	10.12*8.854x10^{-12}

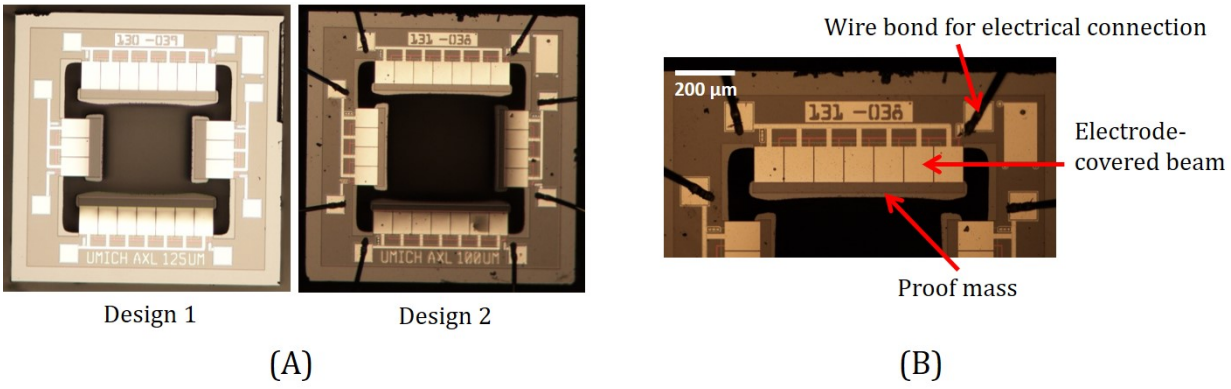

Figure 3.1: Photographs of Design 1 and Design 2 MEMS die. In A), samples of Design 1 and Design 2 are shown with four electrically-independent sensors within each frame. Note that the photograph of the Design 2 die was taken after wirebonds were attached to the electrode pads. In B), a magnified picture of the beam under test is labeled to indicate the beam, proof mass, and wirebond locations.

The general abbreviated process flow is provided in Fig. 3.2. Starting with an approximately 400 µm thick Si wafer, 10 µm thick silicon dioxide (SiO_2) layers are grown on the top and bottom surfaces. Alternating layers of 20 nm thick molybdenum (Mo) electrodes and 0.5 µm thick AlN are deposited on the top side of the substrate. Each of the three electrode layers must be patterned and etched before the subsequent AlN deposition. Then vias are etched in two steps, first to access the middle electrode layer and second to access the bottom electrode layer. Aluminum-copper alloy electrode material is deposited and etched to

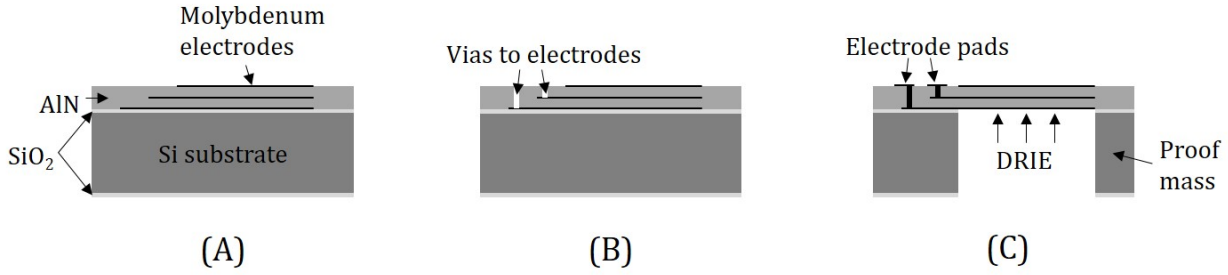

Figure 3.2: Abbreviated process flow for microfabrication, not drawn to scale. In A), alternating layers of Mo electrodes (20 nm) and AlN piezoelectric material (0.5 µm) are deposited on a Si wafer substrate (400 µm) that was covered by a SiO_2 isolation layer (10 µm). In B), vias are defined to access and connect these electrode layers for the desired output. In C), electrode pads are deposited and DRIE defines the frame, beam, and proof mass and releases individual MEMS die.

create electrode pads (to which wirebonds are connected for voltage output). Finally, deep reactive ion etching (DRIE) from the backside of the wafer is used to define the frame and proof mass structures (made primarily of silicon after etching), remove the SiO_2 from the underside of the beam, and to release the device from the wafer. The interested reader is directed to Knisely, *et al.* [42] and Zhao, *et al.* [43] for more detailed information regarding the fabrication process for similar layered AlN beams.

3.2 Experimental Procedures and Results

In this section, the experimental procedures for testing piezoelectric material parameters and characterizing sensor performance are described. These procedures, and the order in which they are completed, have been used historically to test the MEMS devices that have been developed in our group.

In order to test the sensitivity and noise of the piezoelectric vibration sensors, the voltage output is sent through an amplification circuit. This is imperative for three reasons. First, the voltage output from MEMS piezoelectric sensors is often small. For instance, a device with a capacitance of 30 pF experiencing a 1 m/s^2 acceleration input generates a voltage output on the order of 150 µV. Amplifying the output ensures that the signal resulting from smaller input accelerations is not buried in the noise of the data acquisition system (DAQ) or by electromagnetic interference. Second, due to their capacitive nature, piezoelectric transducers produce a high output impedance that does not match the (often lower) input impedance of the DAQ. Without a circuit to facilitate impedance matching, the sensor signal power will be dissipated aross the large impedance and leave little to be detected by the DAQ. Third, additional amplification of the sensor noise will decrease the influence of the DAQ noise on the measured total noise output (each contribution is summed in an RMS sense and includes a specific gain at the output of the circuit). For this work, a simple amplification circuit is implemented with off-the-shelf components and custom printed circuit boards (PCBs). Specific details about the circuit are given below in Section 3.2.1. The

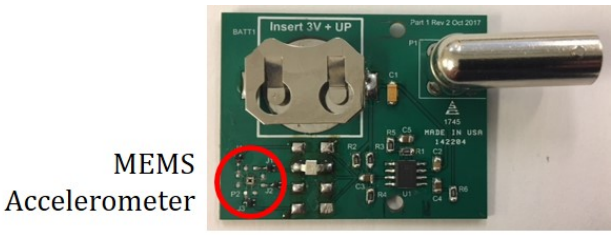

Figure 3.3: A sample amplifier circuit on a printed circuit board. Off-the-shelf surface mount components are soldered onto the pad layout (the largest items are the coin cell battery holder and the BNC connector at the output). The MEMS die is adhered to the PCB with glue and connected to the pads on the board with wirebonds. This layout was not designed to meet any specific size parameters.

manufactured and assembled amplifier is pictured in Fig. 3.3 with the MEMS accelerometer placement location highlighted.

Two National Instruments multifunction input/output devices (PCI-6251 and PXI-6123) controlled with LabVIEW based programs generate the driving signal and obtain voltage data during our experiments. BNC-2110 adapters connect to the PCI-6251 and PXI-6123 to provide ports to connect analog outputs and inputs, respectively. The LabVIEW program creates a 1 second long chirp signal over a user-specified frequency range at a user-defined amplitude. This program is used to test the gain and phase of amplifier circuits, for device voltage actuation, and for sensitivity testing. A second LabVIEW program is used to obtain the averaged output noise spectral density from the piezoelectric devices and circuits.

3.2.1 Amplification Circuit Gain and Phase

Circuits designed for piezoelectric sensors, particularly MEMS devices that have very low capacitance because they are physically small in size, utilize junction field effect transistors (JFETs) at the input. JFETs are high-input-impedance devices that match well with the piezoelectric sensor. When the JFET is configured as a common source amplifier (CSA), it behaves as a voltage-controlled current source which has a low-impedance load. Therefore, it provides some amplification and decreases the impedance at the output; at this point, additional gain and filtering can be easily applied to the signal with operational amplifiers

and passive circuit components. Conveniently, all of the components are easily modeled in SPICE (simulation program with integrated circuit emphasis) or with analytic equations.

Adequate amplification of the signal is achieved with two consecutive stages, although more can be added if needed. The first stage comprises a Panasonic model 2SK3372 JFET configured as the aforementioned CSA. The second stage is a noninverting amplifier consisting of an Analog Devices, AD8655 operational amplifier and a resistive feedback network. First-order low and high pass analog filters are included to define the frequency range of the amplifier and to prevent aliasing of high-frequency noise at the DAQ. These components are placed on a PCB for testing (again, see Fig. 3.3; note that the circuit testing occurs before the MEMS die is added to the PCB). Figure 3.4 shows the simulated (dashed black line) and experimental (red line) frequency response (gain and phase) of the circuit. The experimental data is obtained by sending a 50 mV amplitude chirp signal through the circuit at the input (gate of the JFET), and the model considers the same stimulus. Close matching of these results indicates that the circuit is performing as expected. It has a gain of 33 dB and a -3 dB cutoff frequency of 6 Hz. Data provided shows up to 20 kHz, which is less than the anti-aliasing (low-pass) filter cutoff frequency of approximately 240 kHz. This experiment

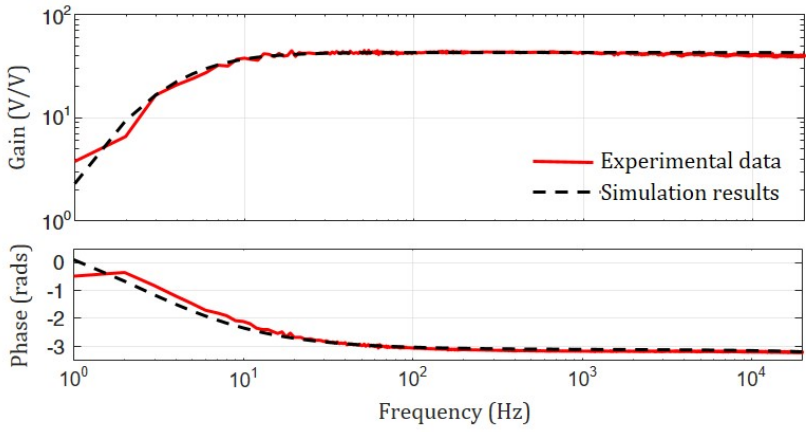

Figure 3.4: Simulated and experimental gain and phase of the amplification circuit. A 50 mV chirp signal was sent to the gate of the JFET and the output of the circuit was connected to the DAQ. The resulting gain is approximately 43 V/V or 33 dB. The -3 dB cutoff frequency for the high-pass filter is 6 Hz.

confirms that the circuit is functioning as expected and it can be used to remove the applied gain in subsequent processing of sensitivity and noise output data, referring all information to the input of the circuit.

3.2.2 Capacitance and Dissipation Factor

Prior to attaching the output of the transducer to the amplifier input, several tests are performed to characterize the sensor. First, the capacitance of the sensor and the dissipation factor (tanδ) of the piezoelectric material are measured. The actual capacitance is needed not only to accurately model the system, but also to determine the amount of stray capacitance on the MEMS die (the difference between the calculated nominal capacitance and the measured value). The stray capacitance that creates a voltage divider and decreases the voltage output from the sensor. It is necessary to measure and account for this value to confirm matching between the sensitivity model and data. $\tan\delta$ is pertinent to accurate sensor noise modeling, and it will vary depending on the quality of the deposited piezoelectric films.

To measure these parameters, we use a Keysight E4980A Precision LCR Meter. To achieve precise measurements, two matched BNC cables are connected in a shielded two-terminal pair configuration. Consult the Keysight documentation for additional information about the connection types and rationale [75]. Electrode pads on the transducer die are accessed with probe tips connected to tri-axial manipulator stages (SemiProbe, Vermont). Measurements are taken with a 1 V signal at 1 kHz using the parallel circuit mode of the LCR meter with capacitance and dissipation factor outputs. The auto-range and long measurement time settings are also chosen. Several measurements are taken on the same device to ensure repeatability and proper electrial connection with the probe tips. At this frequency, the tested sensor has a capacitance of 30.42 pF and a $\tan\delta$ of 0.15%. The expected value of the device capacitance was 25.1 pF, so there are about 5.3 pF of stray capacitance on the MEMS die, the majority of which comes from the 10 µm overlap of AlN and electrode material at the frame and proof mass (dictated by the fabrication process).

The low dissipation factor indicates that the AlN films are high quality [67] which is desired for minimizing the inherent sensor-generated noise.

3.2.3 Voltage Actuation

The second sensor characterization test is voltage actuation which is used to determine the piezoelectric coefficient, d_{31}, of the material. This parameter also depends on the quality of AlN film deposition; it will likely deviate from the nominal value and will affect the sensitivity of the accelerometer (see Eq. 2.22). Littrell and Grosh [70] established a procedure for determining d_{31} by measuring the deflection of piezoelectric beams in response to an applied voltage. This process has been effectively demonstrated with cantilever beams, circular diaphragms [45], and now cantilever beams with proof masses.

A schematic diagram of the actuation experimental set-up is given in Fig. 3.5. With the probe tips placed on the MEMS die electrode pads, the voltage signal (sent as a chirp from the program mentioned above) drives the sensor. A laser Doppler vibrometer (LDV, Polytec Inc., USA) is focused at the end of the beam (at x = L) to measure the vibration where the largest deflection is expected. The LDV output is sent to the DAQ as a voltage signal that is proportional to the velocity of the measurement location. The amplitude and phase of the

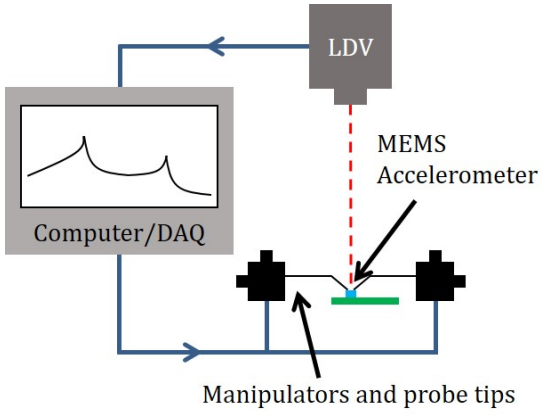

Figure 3.5: Diagram of the actuation experiment configuration. The chirp voltage signal is sent from the driver to the pads on the accelerometer die through the probe tips used to access the electrode pads on the MEMS die. The LDV focused at the end of the beam detects vibration and sends a voltage signal back to the DAQ.

results are computed with the complex-valued data that are easily converted to displacement or acceleration in the frequency domain.

The voltage actuation data are plotted in red in Fig. 3.6. For reference, at 100 Hz the acceleration at the end of the beam is 23.8 mm/s^2 (or 2.43 mg) for 1 V applied to the device. Following the procedure from Littrell and Grosh [70], the d_{31} value is increased until the modeled low-frequency acceleration (black dashed line) matches the collected data. For this sensor, d_{31} is found to be -2.0 pC/N.

While testing this device, we observed that the proof mass is not completely etched (see Fig. 3.1B) and is larger than the designed (as-drawn) dimensions. This is due to the decreased level of control that we have over the etching processes since the devices were not fabricated in-house. Although this does not affect the low-frequency acceleration, adjusting the mass dimensions will bring the resonant frequency prediction in accordance with measured results. Therefore, we increased the proof mass length in the model by 13 µm to 63 µm and the width by 40 µm to 740 µm. This process was used to fit the the data shown in Fig. 3.6 where the first resonance of the model and data occurs at 1420 Hz. Using these data-fit parameters, the model can accurately predict the sensitivity of the fabricated sensor.

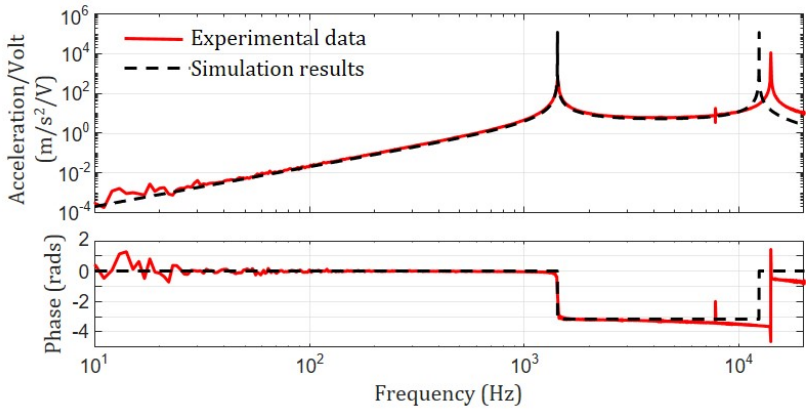

Figure 3.6: Simulated and experimental voltage actuation amplitude and phase of the sensor. A 1 V chirp driving signal was sent to device and the acceleration of the beam was measured using an LDV focused at x=L. Low-frequency fluctuations (from 10 to 30 Hz) are due to the amplifier chosen to drive the high-impedance sensor. The acceleration amplitude is 23.8 mm/s^2 at 100 Hz, resulting in a data-fit d_{31}=-2.0 pC/N. Proof mass dimensions of L_M=63 µm and b_m=740 µm fit the first resonant frequency of 1420 Hz.

3.2.4 Sensitivity

As discussed in the modeling Section 2.3.2, the sensitivity is the voltage output with respect to acceleration input. Once the initial measurements for the capacitance, dissipation factor, and piezoelectric coefficient are complete, we prepare to test the device sensitivity. Referring again to Fig. 3.3, the MEMS accelerometer is glued to the PCB for these experiments. Then the sensor is connected to the input of the amplifier circuit at the JFET with wirebonds (completed at Protoconnect, LLC in Ann Arbor, MI). The schematic for the sensitivity experimental set-up is given in Fig. 3.7A; the diagram illustrates the sensor-carrying PCB secured to an aluminum fixture and attached to the Brüel and Kjær Type 4809 vibration exciter. A photograph of this portion of the set-up is given in Fig. 3.7B. The chirp program that was used for actuation testing is again employed to send a voltage signal to a power amplifier (Brüel and Kjær Type 2706) that drives the vibration exciter. Meanwhile, the LDV is focused on the frame of the MEMS die to measure the velocity it experiences,

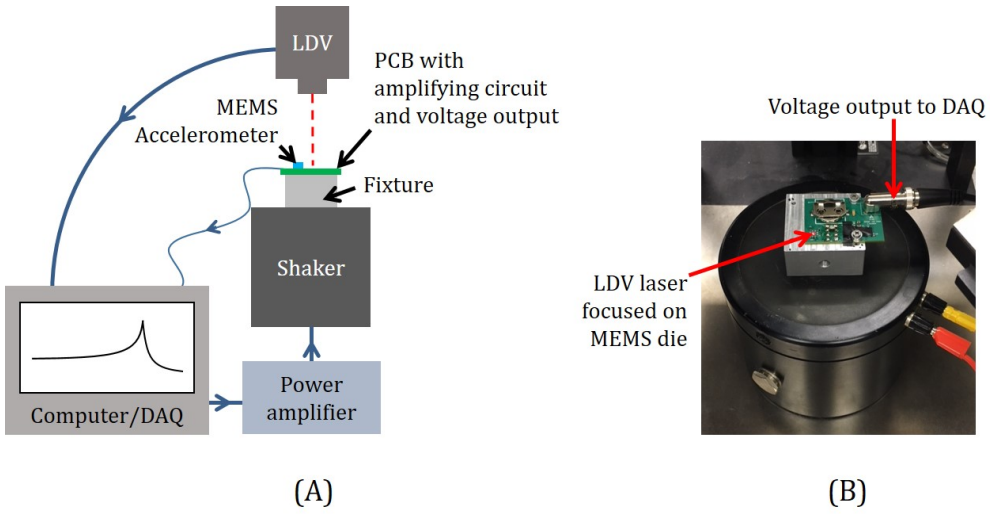

Figure 3.7: (A) Schematic diagram of the sensing experiment set-up and (B) image of the PCB attached to the vibration exciter. The driving chirp voltage signal is sent to a power amplifier that drives the vibration exciter. The MEMS die on the PCB is attached to a fixture that is then coupled to the vibration exciter. The amplified voltage output from the device is sent to one DAQ input and the LDV-measured excitation of the die frame is sent to another DAQ input. These data sets are used to compute the transfer function of the sensor.

and the voltage output from the sensor is amplified by the circuit and measured by the DAQ analog input. The complex-valued sensor voltage data and the LDV voltage data provides the necessary information to calculate the amplitude and phase of the sensitivity transfer function.

Figure 3.8 compares the model-predicted sensitivity (dashed black line) to the measured sensitivity (red line) of the beam under test, converted to units of mV/g. The modeled low-frequency sensitivity is 1.3 mV/g at 100 Hz, which does not include the 33 dB gain from the amplifier circuit but accounts for voltage attenuation caused by stray capacitance. The data shows a maximum deviation from the model of -3 dB at 151 Hz. Otherwise, experimental results lie within ±3 dB of the modeled values up to 900 Hz.

3.2.5 Input Referred Noise and Minimum Detectable Acceleration

In Chapter 2, the sensitivity and noise were modeled solely for the piezoelectric sensor. For that calculation, the noise contribution is called "input referred"; in other words, the value is referred to the input of the circuit, rather than the output of the circuit. Any noise source can be referred to any node of the circuit, as long as the gain from that point to the

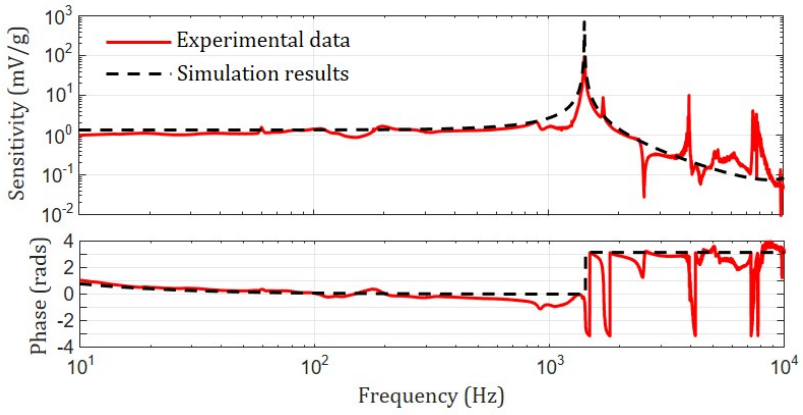

Figure 3.8: Simulated and experimental device sensitivity amplitude and phase. The device is driven by a shaker and the imparted acceleration is measured with the LDV. The voltage output through the amplifier is sent to the DAQ. Accounting for stray capacitance in the system, the low-frequency sensitivity at 100 Hz is 1.3 mV/g (not including amplifier gain). The maximum difference between the modeled and measured result from 10 to 900 Hz is -3 dB at 151 Hz.

output of the circuit (at the measurement location) is known. For instance, when a circuit is included for experimentation, the device noise is amplified by the applied gain where it is measured at the circuit output. So, to refer the measured noise to the input, one has to divide by the gain. Unfortunately, circuit noise sources also contribute to the measured noise at the output. These additional noise sources, while not generated at the input of the circuit, can alto be referred to the input of the circuit. There, all noise sources are summed as RMS voltages. The minimum detectable acceleration (MDA) can be calculated with any sensitivity and noise that are referred to the same point (i.e. they have been amplified by the same gain, so the gain completely cancels in the MDA calculation). Since the sensitivity data presented above in Section 3.2.4 do not include the circuit gain, the noise data presented in this section will be input referred, and the MDA will be calculated with both input referred data sets.

The output noise spectral density of the sensor is measured experimentally by sampling the voltage output from the system with the DAQ and computing its power spectral density. The PCB carrying the sensor and circuit is placed inside a grounded metal box to shield it from electrical interference and on a heavy block to minimize vibration interference. As mentioned previously, an anti-aliasing filter was added before the input to the DAQ since the white noise extends beyond the system sampling frequency of 500 kHz. Again, the measured noise spectral density includes not only the amplified noise from the sensor, but also the noise sources from the amplifier circuit elements.

The total input referred noise (IRN) spectral density, determined by dividing the output noise by the circuit gain, is provided in red in Fig. 3.9 with values in $V/\sqrt{Hz}$ indicated on the left axis. Increased noise levels from 20 to 40 Hz are caused by external vibrations affecting the test set-up, verified by independent accelerometer measurements, and the peak at 1420 Hz is due to the resonance of the sensor. The IRN (in a 1 Hz bandwidth) is 36.3 $nV/\sqrt{Hz}$ at 100 Hz and 11.8 $nV/\sqrt{Hz}$ at 1 kHz.

In the noise model discussed in Section 2.3.4, only electrical-thermal noise from the

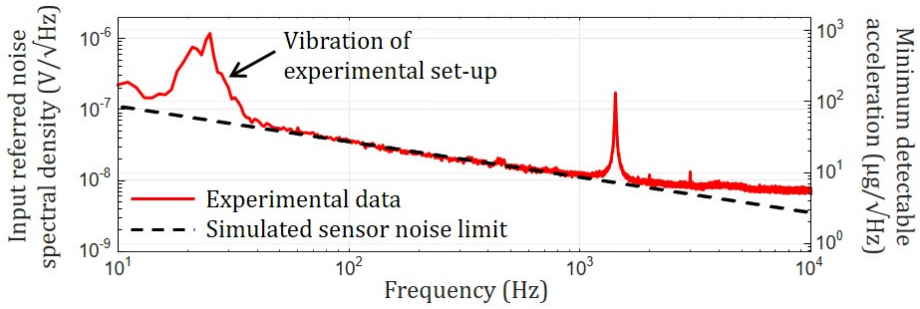

Figure 3.9: Simulated and experimental input referred noise spectral density (left axis) and minimum detectable acceleration assuming constant sensor sensitivity (right axis). The PCB is placed in a grounded metal box on a heavy block to prevent electrical and vibration interference. An anti-aliasing filter with a corner frequency of 240 kHz was added before the DAQ. Complete vibration isolation was not achieved, as indicated by the increased output from 20 to 40 Hz and the resonant peak appearing at 1420 Hz. From approximately 50 to 1 kHz, the modeled and measured noise values match, dictated by tanδ of 0.15%. Input referred noise spectral density of 36.3 nV/$\sqrt{\text{Hz}}$ and 11.8 nV/$\sqrt{\text{Hz}}$ is measured at 100 Hz and 1 kHz, respectively, corresponding to minimum detectable acceleration of 28 μg/$\sqrt{\text{Hz}}$ and 9.1 μg/$\sqrt{\text{Hz}}$.

transducer is considered. The black dashed line in Fig. 3.9 is the contribution of the modeled sensor noise from Eq. 2.18 to the total noise, calculated with the measured $\tan\delta = 0.0015$. As it is an inherent sensor property, we consider this to be the lower limit of the noise floor. The intersection of the modeled and measured noise from 50 Hz to 1 kHz illustrates this limit. Below and above this frequency range, the increased noise floor is due to the circuit elements used to amplify the signal (see [76] for additional information about the contribution of various noise sources in this system).

Finally, we calculate the MDA of the system using the IRN and the constant, low-frequency device sensitivity (1.3 mV/g) according to Eq. 2.19. The resulting spectral values, in units of μg/$\sqrt{\text{Hz}}$, are indicated for the red line in Fig. 3.9 by the right axis on the plot. At 100 Hz and 1 kHz, the MDA is 28 μg/$\sqrt{\text{Hz}}$ and 9.1 μg/$\sqrt{\text{Hz}}$, respectively, calculated with the noise in a 1 Hz bandwidth.

3.3 Discussion

Overall, as evidenced by the results presented above, the analytic models accurately represent the fabricated sensor behavior up to and including the first resonant frequency. Additionally, measured AlN properties (dissipation factor and piezoelectric coefficient) indicate that high quality films were deposited during fabrication [42, 67]. In the remainder of this section, the performance of the tested sensor is discussed with respect to the application-specific requirements discussed in Section 1.3.2. By increasing the resonant frequency of the now validated model, this sensor concept can be fairly compared to other devices and assessed with a larger bandwidth.

3.3.1 Mapping Input Sound Pressure Level to Acceleration

To effectively discuss the performance of this sensor, we first need to map the minimum detectable signal requirement from sound pressure levels (dB SPL) to acceleration values (in m/s^2 or g). Conveniently, studies of human middle ear mechanics have provided velocity data for various ossicle measurement locations in response to acoustic stimuli. Within the dynamic range considered in this work, the behavior of the ossicular chain is assumed to be linear. Therefore, normalized motion data (displacement, velocity, or acceleration) can be scaled to any input level. In the example conversion described here, we use data from Sachse et al. [51], that is presented as averaged data from Goode et al. [77], for umbo displacement measured with a 30 dB SPL stimulus.

First, the displacement data must be converted to acceleration data and normalized to the input stimulus in Pascals (Pa) In the frequency domain, and assuming harmonic forcing, the displacement data is multiplied by a factor of ω^2 to obtain acceleration values. By definition, the input stimulus of 30 dB SPL is equal to 632.5 µPa; the acceleration data will be scaled by this value to find acceleration sensitivity in units of $m/s^2/Pa$. Then, recalling the hearing threshold and equal-loudness-level contours presented in Section 1.3.2, each point is a dB SPL value that alto gets converted to Pa. Finally, the acceleration sensitivity at each

frequency is multiplied by the pressure, resulting in hearing threshold and loudness contours as accelerations (m/s^2). This process was completed for the previously plotted data, which is now presented in Fig. 3.10. With additional data sets, this conversion can also be done to assess other attachment locations for the sensor.

3.3.2 Performance of the Fabricated Sensor

As mentioned in Section 3.1, we were alotted a particular die size for this fabrication process. Therefore, the volume of a fabricated sensor die is 0.8 mm^3 (1.4 mm x 1.4 mm x 0.4 mm). This volume does not exceed 3 mm, but the MEMS die is not the only component that will be packaged for the device. Integrated circuits necessary for signal conditioning will be placed close to the piezoelectric sensor within a package housing. Considering that a single beam/mass pair only occupies 0.9 mm x 0.4 mm x 0.4 mm, even more space is conserved. Similarly, the total mass of the die is approximately 1.2 mg, but the single-sensor

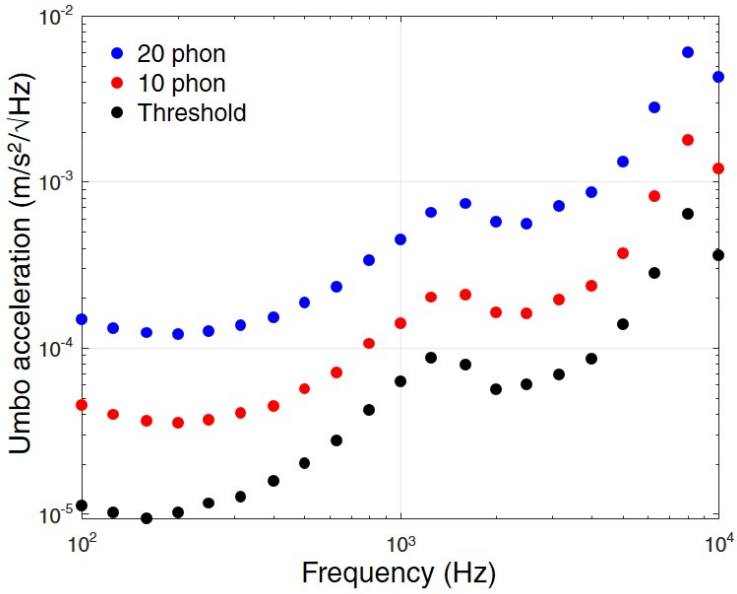

Figure 3.10: Hearing threshold and two equal-loudness-level contours (10 and 20 phon) converted to equivalent umbo acceleration values. Hearing threshold data points (black), and 10 phon (red) and 20 phon (blue) data points that were presented in Chapter I are converted to present the minimum detectable signal specification as acceleration that can be directly compared to sensor data.

section would only be 0.25 mg. With additional silicon components (the integrated circuit chip), a package housing, wires, and glue, we predict that this accelerometer will be less than 13 mg (less than the average mass of the malleus or incus at 30 mg [8]).

The bandwidth of the tested sensor reaches approximately 900 Hz, falling far short of the application bandwidth specification of 8 kHz. In this case, the frequency range was limited by the conservative dimensions chosen and the processes used to fabricate the sensor. The large proof mass drove down the resonant frequency, and while shortening the beams would have increased it again, a narrower gap between the vertical side walls of the frame and mass caused etching aspect ratio concerns. In future design iterations it will be necessary to both shorten the beams and decrease the size of the proof mass to sufficiently increase the bandwidth of the system. Although the full dynamic range of the sensor was not tested explicitly, the level of excitation applied by the shaker at 1 kHz is about 113 dB SPL. This level is determined by calculating the pressure in Pa that would be needed to achieve the measured acceleration value (using the same data from Section 3.3.1) and converting it to dB SPL. Since the transfer functions of both the middle ear response and the applied shaker acceleration amplitude vary with frequency, the sound pressure level is not constant with frequency; 1 kHz is chosen for convenience.

To facilitate comparison, the information presented in Figures 3.9 and 3.10 is combined in Fig. 3.11, with the sensor MDA data plotted in $\mathrm{m/s^2}/\sqrt{\mathrm{Hz}}$ instead of $\mu\mathrm{g}/\sqrt{\mathrm{Hz}}$. As can be seen in these results, the sensor MDA is lower than the threshold levels of acceleration from approximately 3 kHz to 10 kHz, it is lower than the 10 phon values from about 800 Hz to 10 kHz, and lower than the 20 phon contour from nearly 300 Hz to 10 kHz. However, based on the resonant frequency the upper limit to the accelerometer bandwidth is currently around 900 Hz. So, despite exceeding threshold requirements above 3 kHz, the device sensitivity is not constant over this range. Over the spans were the sensor achieves 10 and 20 phon acceleration limits, the resonant frequency will cause a phase shift in the signal, and the sensitivity will not be constant after the resonance.

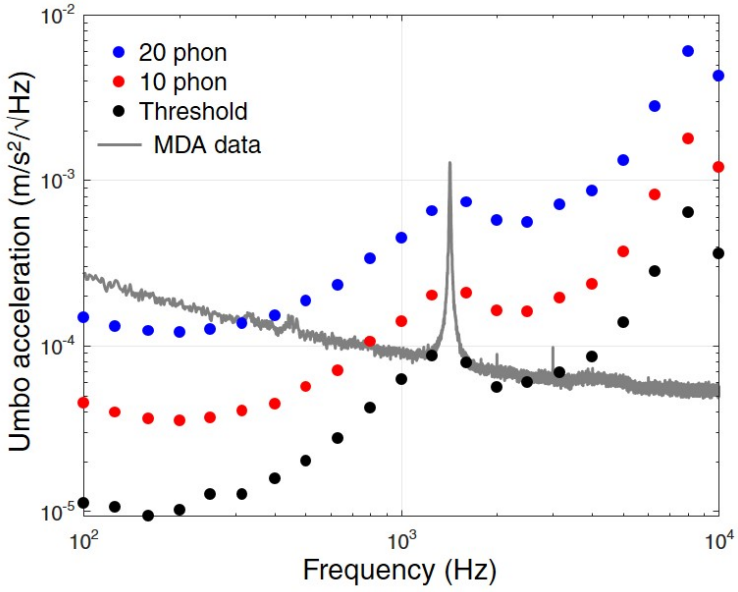

Figure 3.11: Hearing threshold and two equal-loudness-level contours (10 and 20 phon) converted to equivalent umbo acceleration values. Hearing threshold data points (black), and 10 phon (red) and 20 phon (blue) data points that were presented in Chapter I are converted to present the minimum detectable signal specification as acceleration that can be directly compared to sensor data.

To achieve constant sensitivity and phase over the desired bandwidth, the resonant frequency of the device must be increased to approximately 15.4 kHz (resulting in a 3 dB bandwidth of 8 kHz). In this case, a beam length of 50 µm and a mass length and thickness of 85 µm and 50 µm, respectively, would generate a wide enough bandwidth. Within a die area of 2.2 mm x 2.2 mm, which we assume could be packaged within a reasonable total volume, 12 2 mm wide beams can be arranged; the resulting sensor can detect 20 phon acceleration levels from 500 Hz to 8 kHz. We conclude that a single-resonance piezoelectric cantilever cannot achieve the bandwidth and MDA requirements (within reasonable package dimensions) for this application.

3.3.3 Comparison of the Fabricated Sensor with a Capacitive Device

The MDA equation not only permits efficient sensor design, but also allows us to compare this sensor to other devices published in the literature. By altering the dimensions to match

the resonant frequency of a reference accelerometer and calculating the MDA, the results can be compared fairly (i.e. one sensor would not have better performance due to a higher sensitivity created by a lower resonant frequency). For example, the capacitive accelerometer presented in [50] has an approximate spectral MDA value of 87 µg/$\sqrt{\text{Hz}}$ at 200 Hz and a resonant frequency of 6.44 kHz. For our piezoelectric device design, the simplest way to increase the resonant frequency of the device is to decrease the thickness of the mass. If the mass is 150 µm thick, a 50 µm long beam and a 85 µm long mass create a resonance at 6.6 kHz In this case, the beam need only be 340 µm wide to achieve the same MDA as the capacitive sensor. Put another way, if we use an active sensor area of 1 mm^2 as in [50], wherein we fit four 700 µm wide beams, the MDA is decreased to 30 µg/$\sqrt{\text{Hz}}$ at 200 Hz. For the implantable sensor application where meeting both size and MDA specifications is imperative to device success, this demonstrates the increased efficacy of the piezoelectric sensor design.

3.4 Conclusion

In this chapter, we seek to validate our analytic models with experimental data from fabricated accelerometers. Fabricated MEMS devices do not always identically match the as-drawn design, especially when the fabrication processes are not optimized to the device configuration or geometry. Additionally, properties of deposited piezoelectric materials are variable, and some of the model parameters must be fit with tests directed at isolating and identifying a specific variable. Here, the device capacitance, dissipation factor, and actuation response are characterized; furthermore, mass dimension adjustments are made to align modeled and measured resonant frequency. These experiments are used to calculate the stray capacitance on the MEMS die and to determine d_{31} of the deposited piezoelectric material for the sensitivity model, and to fit the noise model with the proper loss tangent.

Due to conforming to fabrication process requirements, the device design was not intended to meet the specifications for measuring ossicle vibration discussed in Chapter I. However,

the performance of the sensor in the context of that application is described. In a direct comparison to the hearing threshold and equal-loudness-level contours, the sensor appears to perform decently, but the location of the resonant frequency peak and phase shift in the sensitivity negates the design as a realistic possibility. While piezoelectric sensing is shown to more effectively meet size and MDA requirements simultaneously than capacitive sensing does, it is also concluded that a single-resonance design is not a feasible solution to meet all of the needs of ossicular vibration sensing.

CHAPTER IV

Alternative Accelerometer Designs: Multi- and Dual-resonant Piezoelectric Sensing

Sensors are most commonly designed with an operational bandwidth that lies in the sub-resonance, constant sensitivity region of the device, which is the approach we take in this work up to this point. However, as discussed in Chapter III, the piezoelectric accelerometer designed with a single resonant frequency is not able to simultaneously meet all of the necessary requirements for implantation and sensing in the middle ear. Hence, in this chapter, we propose an alternative approach that involves multiple sensing elements within one device. The work presented in this chapter is model-based; these device designs have not yet been fabricated for experimental testing. Based on the theory, and according to our best knowledge, the proposed sensor will be the best-performing middle ear accelerometer in the literature.

4.1 Multi-resonant Piezoelectric Accelerometer

4.1.1 Design Concept

Multi-resonant sensors, or sensors that have individual elements contributing different sensitivity values and resonant peaks in the sensitivity spectrum, are not a new concept. In fact, this approach is attractive for piezoelectric energy harvesting wherein the high

sensitivity and quality factor around a system resonance permit efficient energy transfer [78, 79, 80, 81, 82]. This idea is also used in the context of designing intracochlear pressure transducers and artificial basilar membrane devices that mimic the tonotopic mapping of the cochlea [30, 42, 44, 45, 83, 84, 85, 86]. In these systems, one sensing element will contribute maximally to teh measured of processed sensor output. In the case of a multi-resonant accelerometer, the increased sensitivity that can be achieved with the resonant peaks is desirable, but not at the cost of a smooth (i.e. constant) sensitivity and predictable phase throughout the working bandwidth.

The piezoelectric beams studied in this work provide many variables that can be manipulated to tailor the frequency response of a sensor. As seen in previous chapters, the physical dimensions alter the resonant frequency and sensitivity; in other words, the frequency peak can be precisely tuned as desired. Furthermore, the concepts mentioned briefly in Section 2.2.2 regarding the series/parallel, in/out-of-phase connections can be employed for the purposes of obtaining a unique sensor voltage output. Removing or adding additional electrode material on beam can be used to create on-die voltage dividers to attenuate some signals as well. These examples constitute analog methods to control the sensitivity of the sensor that will be used to either extend the frequency range to include the system resonant frequencies, or to create a band pass region of high sensitivity. Both of these scenarios will be discussed below in Section 4.1.2.

A perspective diagram of an example multi-resonant accelerometer concept is illustrated in Figure 4.1. An array of eight piezoelectric bimorph beams of increasing length with end masses are all connected to the same frame. Any number of beam/mass pairs can be included in this system; however, since there are typically size constraints imposed on the design, the overall MEMS die size should be considered. The electrical connections demonstrate parallel connection of all of the beams, but this is not required for the theoretical design. Again, in the most general case, every physical dimension of the beams and masses can be varied, but this is not practical in terms of MEMS fabrication ease. Controlling the number

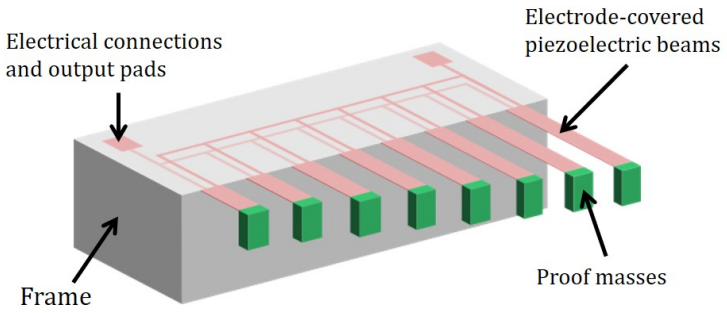

Figure 4.1: A perspective-view diagram of the multi-resonant accelerometer. Eight piezoelectric bimorph beams with independent proof masses are anchored to the same frame. They will all experience the same acceleration input, but the voltage output will depend on the dimensions of each beam/mass pair.

of variables, whether by assuming that each beam is the same thickness (same number of piezoelectric/structural layers) or that the proof mass thickness will be constant across the array, reduces fabrication complications but still allows for significant control over the sensitivity outcome.

4.1.2 Modifications to the Analytic Model

The sensitivity of each beam in the array is modeled as described in Chapter II with the uniaxial stress constitutive hypothesis (since beams in an array of sensing elements will likely be narrower). A minor change to the model is the necessary addition of damping which is used to smooth out the sharpness of the resonant peaks in the spectrum. Damping also contributes to phase shifts that prevent nulls in the frequency response due to cancellations in voltage output. Viscoelastic damping is included by defining a complex elastic modulus as $E^* = E(1 + \eta j)$. In these models, $\eta = 0.1$ is applied to each beam. More sophisticated damping models can be implemented as needed, or simulated in a finite element solution. In the physical system, additional damping can be created by fabrication with parylene coating, for example.

4.1.3 Results for an Example Multi-resonant System

Figure 4.2 demonstrates modeled results for an example multi-resonant device and a single-resonant comparison. The multi-resonant sensor consists of five beams that are 100 µm wide and increase in length from 400 µm to 600 µm in 50 µm increments, and are electrically connected in parallel. All five masses are 50 µm long, 100 µm wide, and 100 µm thick. The reference single-resonant accelerometer design has a 150 µm long beam that is 500 µm wide, and a 50 µm long and 100 µm thick proof mass. Figure 4.2A are the sensitivity and phase plots for each design, and Fig. 4.2B is the minimum detectable acceleration for each.

The single-resonance sensor model output, plotted in red, exemplifies the typical method for defining the bandwidth in the linear, low-frequency region of frequency response. Under these conditions, there is no way to increase or amplify the sensitivity without also amplifying the output noise; therefore, the MDA of this device cannot be lowered without any physical modifications. In-phase connections are of the multi-resonant sensing elements are plotted in green. The results for this case are very intuitive - the outputs are summed across the entire frequency range. Out-of-phase connections are employed in the alternating phase case, where each beam is connected out-of-phase with the beams next to it in the sensing element

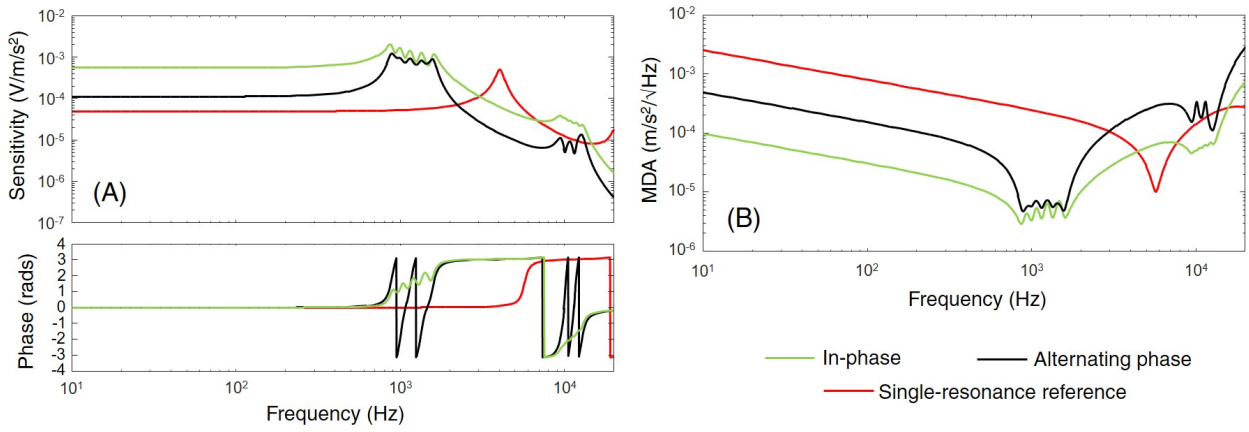

Figure 4.2: (A) The sensitivity and phase and (B) the MDA for a modeled five-resonance sensor and a reference single-resonance sensor. The green curve illustrates the in-phase connection of the five beams and the black curve illustrates the same beam outputs connected with alternating phases. The red curve for the single-resonance case demonstrates the conventionally designed maximum sensitivity that can be achieved for a particular bandwidth.

array. As seen in the black curve, this type of connection provides a frequency band of high sensitivity in a band-pass manner. In both cases, the low-frequency sensitivity is improved compared to the single-resonance accelerometer. The multi-resonant designs also generate less noise since they have a larger capacitance than the reference device. The combination of lower noise and higher sensitivity significantly reduces the MDA. The in-phase result decreases the MDA by 29 dB and the alternating phase result decreases the IRN by 15 dB.

The method of in-phase electrical connections is used to increase the low-frequency sensitivity and incorporate the resonant frequency peaks into the usable bandwidth of the sensor. While the green curve in Fig. 4.2A illustrates this potential, the result it is not perfectly smooth. Similarly the band-pass type frequency range for the alternating phase connections is successful, but the spectrum still exhibits distinguishable peaks. This can be improved by adding more beams to the array so that the resonant frequencies are more closely spaced, scaling the output of a beam using analog or digital means, or filtering the response from each beam. Scaling the output in the analog domain may involve intentionally designed stray capacitance to act as a voltage divider and decrease the output voltage or designing series connections of electrodes on a single beam to increase the voltage output. Nevertheless, even without using these tools to manipulate the signal, this example model illustrates the potential of these methods to improve the sensor resolution.

4.2 Dual-resonant Accelerometer

The concepts discussed in the previous section work well in theory, but are difficult to implement in practice. Also, for the input to an auditory signal processor, the ripple in the sensitivity and phase would not be ideal. Inevitably, there will be additional digital signal manipulation despite the analog efforts made with the design. In this section, we scale back this approach to a design with just two sensing elements, each having a different resonant frequency. Each sensing element is designed to cover a portion of the frequency range wherein it meets the MDA specification for 20 phon acceleration levels discussed previously.

In this way, we are able to meet competing demands of MDA, sensor size, and bandwidth. Appropriate filtering and amplification will be incorporated in the analog or digital domains to create a smooth transition from one dominant sensor output to the other and obtain the desired overall frequency response for the sensor.

4.2.1 Design Concept

A top and side views of the proposed transducer structure are given in Fig. 4.3, where the low-frequency sensing element is red and the high-frequency sensing element is blue. We consider that the outputs from each sensor will be handled with analog and digital signal processing, but here we will only discuss the design of each beam/mass pair to achieve the MDA goals of the application. Each sensing element construction follows the same assumptions considered in Chapter II with damping included as stated above in Section 4.1.2 (bimorph beams, parallel layer connection). The schematic demonstrates the expected differences in size of the piezoelectric beams and proof masses, since increasing the dimensions will lower

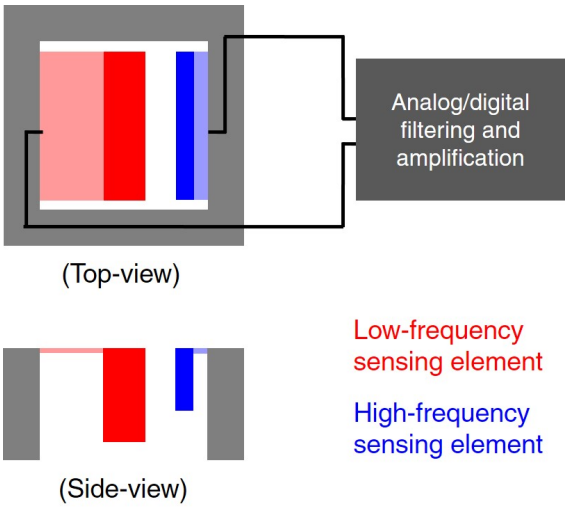

Figure 4.3: A schematic drawing of the proposed dual-resonant sensor concept. A low-frequency sensing element is represented in red, and a high-frequency sensing element is shown in blue. The outputs of each sensor will be filtered and amplified in the analog or digital domain to obtain a smooth transition from one sensitivity to the other. The side view highlights the expected differences in dimensions expected to create the different resonant frequencies and bandwidths.

the resonant frequency.

4.2.2 Results for the Designed Dual-resonant Sensor

The MDA design expression derived in Chapter II was used to determine the dimensions for the two sensing elements. The process was very similar to the case study approaches presented in Section 2.4.3, but required additional iteration. For instance, after choosing a resonant frequency limit to achieve certain bandwidth, the MDA is calculated for the dimension combinations and the best result is chosen. However, if the beam would need to be too wide (say, greater that 1 mm) to decrease the MDA enough to meet the requirement at the lowest frequency in the range, then the result is not feasible. The next iteration would include a lower resonant frequency to aid in MDA decrease, and the beam width would be checked again.

The top-down view of the proposed design dimensions, placed in a sample MEMS die frame, is given in Fig. 4.4. The red-colored, low-frequency range device has a 50 µm long beam and a 250 µm long mass. The beam is 1 µm thick (assumed to be two 0.5 µm thick

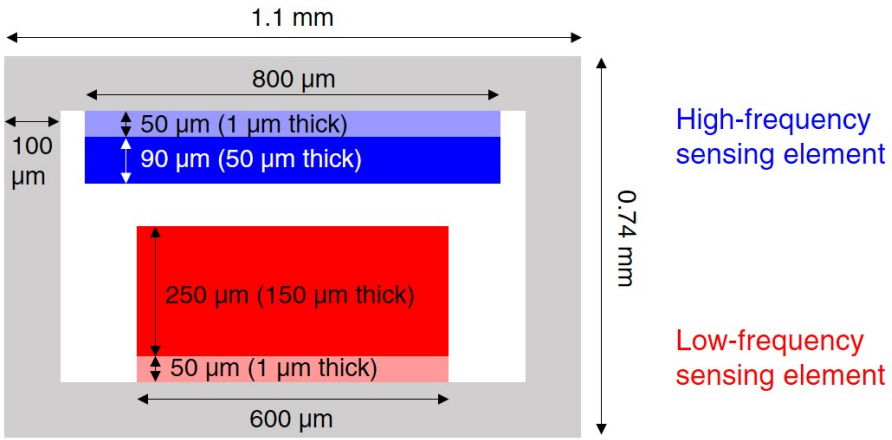

Figure 4.4: Top-down schematic view of the proposed sensor. As in the previous schematic, the low-frequency device is red and the high-frequency sensing element is blue. Each beam and mass is marked with its length and width dimensions, and the thicknesses are given in parentheses. The width of the die frame is chosen as a reasonable MEMS fabrication capability. The beam widths can be made larger, but are represented as the minimum required to meet the desired MDA level. The resulting die area is 1.1 mm x 0.74 mm.

layers) and the mass is 150 µm thick (into the page); both are 600 µm wide. The blue-colored, high-frequency range device has a 50 µm long beam and 90 µm mass that are both also 800 µm wide. The beam is 1 µm thick and the mass is 50 µm thick. These structures are attached to a frame that is 100 µm wide on each side which, in our experience, is reasonable for fabrication of the MEMS devices. The total chip area is 1100 µm by 740 µm. The presented widths illustrate the minimum necessary to meet the MDA specification at the lowest frequency in each range, but they can be increased as die space permits.

The modeled sensitivities for the sensing elements are plotted together in Fig. 4.5, again color-coded to the low (red) and high (blue) frequency ranges. The low-frequency sensor has a sensitivity of 0.445 mV/m/s^2 and the bandwidth extends to 1250 Hz. The sensitivity of the high-frequency component is 25 µV/m/s^2 and its bandwidth extends from 1250 Hz to 8 kHz. If both sensors were 800 µm wide, the noise generated by each sensor would be the same since the beam lengths are the same. However, the 200 µm difference will not significantly increase the noise of the low-frequency sensor; furthermore, the higher sensitivity of the low-frequency beam still creates a much lower MDA for that element.

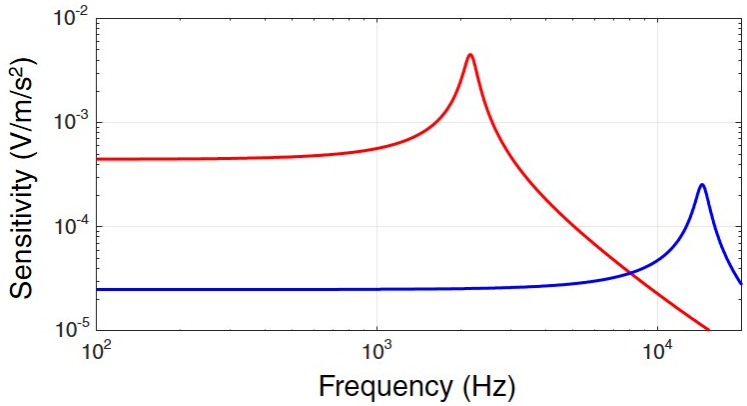

Figure 4.5: The sensitivity of each sensing element, plotted together with consistent colors (red for low-frequency and blue for high-frequency). The device sensitivities at 100 Hz are 0.445 mV/m/s^2 and 25 µV/m/s^2. The first resonant frequency is 2160 Hz, providing a bandwidth of approximately 100 Hz to 1250 Hz. The second resonant frequency is 14.5 kHz, leading to an upper frequency limit of 8 kHz. The lower limit of the range is considered to be where the first sensor range ends, at 1250 Hz.

The resulting MDA spectra for each sensing element in this design is plotted over its effective frequency range in Fig. 4.6, and compared to the previously discussed threshold, 10 phon, and 20 phon acceleration levels. As designed, this total sensor output is predicted to detect the 20 phon MDA levels across the entire frequency range. To our knowledge, this would be the best-performing ossicular vibration detector in the literature. Although this proposed design did not aim for the MDA required to measure 10 phon or threshold level accelerations, the low-frequency sensor can detect them above 517 Hz and 800 Hz, respectively. The high-frequency sensor would function at those levels above approximately 4.5 kHz for 10 phon and 6 kHz for hearing threshold.

4.2.3 Transient Response of Sensing Elements

In practice, a sensed acceleration input to an auditory prosthesis signal processor should have a short rise time (the first time at which the steady-state value is reached) and a short

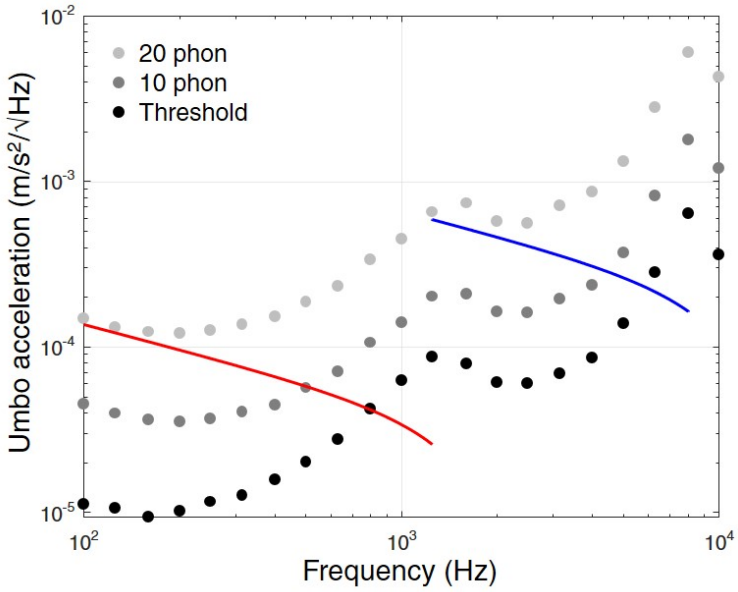

Figure 4.6: Replicated hearing threshold and equal-loudness-level contours (10 and 20 phon) converted to acceleration compared to the sensing element MDA spectra. Again, each sensor is plotted with its corresponding color; it is also plotted over its designated frequency range. The output from this sensor will meet 20 phon equivalent acceleration values, as designed. Over smaller ranges, it will meet the more difficult 10 phon and threshold acceleration levels.

settling time (time at which the response stays within 5% of its steady-state value for all remaining oscillations) [87, 88]. In this section, we estimate the rise time and settling time for each sensing element by considering the underdamped response of a second-order system. In each case, damping is included through a complex elastic modulus (see Section 4.1.2) which needs to be translated to a damping coefficient, ζ. The low-frequency beam has a natural frequency of 2274 Hz and a damped resonant frequency of 2212 Hz. Through the relationship $\omega_d = \omega_n\sqrt{1-\zeta^2}$, we find $\zeta = 0.23$. Similarly, the high-frequency sensor has natural and damped resonant frequencies of 15222 Hz and 15050 Hz, respectively, resulting in $\zeta = 0.149$.

Based on the damping coefficient and the damped natural frequency, the rise time can be calculated as follows:

$$t_r = \frac{1}{\omega_n}\left(\pi - \tan^{-1}\left(\frac{\sqrt{1-\zeta^2}}{\zeta}\right)\right) . \tag{4.1}$$

Additionally, the settling time can be found as

$$t_s = \frac{3}{\zeta\omega_n} . \tag{4.2}$$

Using the damping coefficient calculated for the low-frequency sensing element, the rise and settling time is 0.13 ms and 5.7 ms, respectively. The high-frequency element has a rise time of 0.114 ms and a settling time of 1.3 ms.

4.3 Conclusion

The work presented in this chapter builds on Chapter II and the concepts of combining piezoelectric sensing elements physically and electrically. The proposed dual-resonant design is quite simple; the only difference between this device and what was fabricated and tested in Chapter III is the desired proof mass thickness. Decreasing the mass thickness from full fabrication wafer thickness requires additional process steps that must be accurately

characterized to achieve the desired mass shape.

For this application, two or more resonant elements within a functional sensor appears to be the most promising route to success. We show that small-area devices can be designed to meet low-amplitude acceleration requirements over a wide frequency range. As stated above, the proposed design would be the best-performing sensor in this class of devices researchers have been studying for over 20 years. Furthermore, by adding a few more devices, a sensor design to meet the 10 phon specification may even be feasible. All of this theory relies on a very important factor - that an appropriate and effective cross-over network can be designed and implemented for this system. The noise that the circuit contributes will also affect the results, but the design can be adjusted to increase the MDA margin to account for added noise sources. As this work progresses, circuit design, device fabrication, and experimental testing will have to be completed as they were for the first-generation devices presented in Chapter III. Small form-factor device packaging will also have to be designed, followed by testing in human cadaveric temporal bones to understand how the device will perform in a real-use setting.

CHAPTER V

Conclusions, Contributions, and Future Work

5.1 Conclusions

The aim of this dissertation, and the contributions herein, is to advance completely-implantable auditory prosthesis systems through improved sensing capabilities. Completely-implantable systems have demonstrated benefits over externally worn hearing aids and cochlear implant signal processors (utilization of outer ear function, continuous functionality during daily activities). However, sensing mechanisms that are simple to implant (such as attachment to an ossicle rather than a bone-embedded transducer) and have adequate performance characteristics (large bandwidth, low minimum detectable signal) have yet to be realized. It is imperative to achieve a system performance with which the benefits to hearing capability will outweigh the risks of surgery. This is especially true in cases of hearing loss where electrode implantation in the cochlea is *not* required and invasive middle ear surgery could affect residual hearing. Departing from high-performance electret and MEMS microphones, research into acceleration sensing within the middle ear has been on-going for over 20 years. In this work, we propose a new piezoelectric MEMS accelerometer design based on experimentally-validated theory that holds the potential to meet all of the design requirements for sensing ossicular vibration as the input to an auditory prosthesis.

This work has followed a design-build-test-iterate approach. In Chapter II, the analytic model of the proposed MEMS piezoelectric bimorph accelerometer is presented. From this

model, a minimum detectable acceleration design equation is derived; trends studied with this expression indicate that the piezoelectric beams should be as wide as possible. Increased width is not valid for the original model assumptions, so a new constitutive hypothesis is assumed and both results are compared to a 3-dimensional finite element model. Regardless of the hypothesis used, the design equation is still valid and is used to quickly assess the design space without requiring lengthy finite element simulations, as demonstrated in example case studies.

Chapter III includes the experimental testing of the first fabricated accelerometers. These device designs were fabricated in a collaboration with Vesper Technologies and constrained to certain aspects of their processes. Rather than use the derived design equation with the applied constraints, we chose conservative dimensions to ensure yield of functional sensors. The fabricated devices undergo material property and sensor performance characterization testing, and the results are presented for a tested beam. The results also demonstrate that the analytic models are valid for devices that are subject to realistic fabrication variability. Ultimately, the work to this point elucidates that this piezoelectric accelerometer configuration with a single device resonance will not achieve the all of the requirements for implantation and sensing in the middle ear.

Based on these results, a new concept is proposed in Chapter IV for another design iteration. Multiple system sensitivities and resonances can be employed to tailor the sensor output voltage (typically to improve overall sensitivity). In the new sensor design, two piezoelectric beams are designed to meet the requirements for minimum detectable acceleration over independent frequency ranges within the application bandwidth. The chapter concludes with a proposed design that would be, to our knowledge, the best-performing implantable ossicle vibration sensor for auditory prostheses in the literature.

5.2 Contributions

The contributions of this work are listed below in categories relating to the use of the analytical model, the experimental testing of the fabricated devices, and accelerometer designs.

- Analytic modeling
  - The validated analytic model for the piezoelectric accelerometer system can be used to accurately model the system rather than running lengthy FEA simulations.
  - An even simpler model based on the assumed-mode solution generates the MDA design expression which is demonstrated to assist in rapid assessment of the design space of variables.
  - Analytic models can be used to make fair comparisons to other devices, without requiring identical geometry or the same sensing mechanism, by analyzing the MDA with an identical system resonant frequency.
- Experimental testing
  - The experiments were used to fit the piezoelectric coefficient, illustrating that this method can be used obtain a reasonable d_{31} estimate for a non-ideal geometry.
  - Fabricated devices highlight the need for carefully controlled processing to obtain as-drawn (designed) geometries of the devices.
- Sensor designs
  - A theoretical multi-resonant sensor with two electrical connection schemes was demonstrated to increase device sensitivity over the desired frequency range(s) and decrease the minimum detectable acceleration.

– A dual-resonant sensor is designed specifically to meet the bandwidth, minimum detectable acceleration, and physical size constraints for the target application.

The last contribution regarding the dual-resonant sensor design is the most important outcome of this work. Not only would the device meet a more stringent MDA specification than is pursued in the existing literature, but it also clearly demonstrates the need to shift from single-resonant design concepts to dual- or multi-resonant devices for this application. If the theoretical result is realized in a fabricated MEMS device, we will have reached the acceleration sensing goal that others have sought for two decades, promising significant improvement for sensing in auditory prostheses.

5.3 Future Work

This work concludes at the beginning of another iteration of our design-build-test process; therefore, there is still much work to be done. Building this device will require more precise control over the fabrication process to obtain accurate proof mass geometries and high-quality piezoelectric films. These variables play important roles in achieving the desired frequency response. Another key component is to design a low-noise, low-power circuit that will generate a smooth transition from the output of one sensing element to the other depending on the input signal frequency. The design of an integrated circuit chip for this purpose will require specific expertise. Throughout this system design process, the rise and settling times of the sensing elements must be analyzed more rigorously than the estimates provided in Section 4.2.3. The transient response will indicate the appropriate amount of damping required to eliminate ringing in the processed signal while simultaneously maintaining short delay between the input sound and stimulation of the cochlea.

Many of the accelerometer projects referenced throughout this work also included experimental testing of the sensor in human cadaveric temporal bones. This is an important step in this process as it will inevitably highlight design flaws and additional constraints

that must be considered. To attempt these experiments, the sensor and integrated circuit must be packaged in a small housing to provide protection from the environment and a bone attachment surface. At the time of writing this document, steps on this path have already been taken and will continue to be pursued.

APPENDICES

APPENDIX A

Analytic Model Solutions

A.1 Matrix Elements for Sensitivity Solution

The following expressions are used in Eq. 2.15 in Section 2.3.2:

$$X_1 = (-Y_1 - Y_2)\sin(kL) - Y_3\cos(kL) \qquad X_5 = (-Y_4 + Y_6)\cos(kL) + Y_5\sin(kL)$$

$$X_2 = (-Y_1 - Y_2)\cos(kL) + Y_3\sin(kL) \qquad X_6 = (Y_4 - Y_6)\sin(kL) + Y_5\cos(kL)$$

$$X_3 = (Y_1 - Y_2)\sinh(kL) - Y_3\cosh(kL) \qquad X_7 = (Y_4 + Y_6)\cosh(kL) + Y_5\sinh(kL)$$

$$X_4 = (Y_1 - Y_2)\cosh(kL) - Y_3\sinh(kL) \qquad X_8 = (Y_4 + Y_6)\sinh(kL) + Y_5\cosh(kL)\ .$$

In these terms, Y_1-Y_6 are defined as follows:

$$Y_1 = \overline{EI}k^2 \qquad Y_3 = I_M k\omega^2 \qquad Y_5 = M\omega^2$$

$$Y_2 = \frac{1}{2}ML_M\omega^2 \qquad Y_4 = \overline{EI}k^3 \qquad Y_6 = \frac{1}{2}ML_M k\omega^2\ .$$

All of the variables used in these expressions are defined in Section 2.3.1.

A.2 Matrix Elements for Assumed-mode Sensitivity Solution

The following expressions are used in Eq. 2.21 in Section 2.4.1:

$$\tilde{X}_1 = 6\overline{EI}L - \frac{1}{2}ML_ML^3\omega^2 - 3I_ML^2\omega^2 \qquad \tilde{X}_5 = 6\overline{EI} + ML^3\omega^2 - \frac{3}{2}ML_ML^2\omega^2$$
$$\tilde{X}_2 = 2\overline{EI} - \frac{1}{2}ML_ML^2\omega^2 - 2I_ML\omega^2 \qquad \tilde{X}_6 = ML^2\omega^2 + MLL_M$$
$$\tilde{X}_3 = -\frac{1}{2}MLL_M\omega^2 - I_M\omega^2 \qquad \tilde{X}_7 = ML\omega^2 + \frac{1}{2}ML_M\omega^2$$
$$\tilde{X}_4 = -\frac{1}{2}ML_M\omega^2 \qquad \tilde{X}_8 = -M\omega^2 \ .$$

A.3 Coefficients for Resonant Frequency Calculation

The following expressions are the coefficients of the quadratic equation used to calculate ω_1^2 and ω_2^2 after taking the determinant in Eq. 2.24.

$$\tilde{A} = (\rho_{mass}bL_Mt_M)^2L^4\left(\frac{1}{12}L_M^2 + \frac{1}{3}t_M^2\right)$$
$$\tilde{B} = (\rho_{mass}bL_Mt_M)^2L\left(\frac{bt_{piezo}^3}{s_{11}}\right)\left[\frac{5}{3}L^2 + 4LL_M + \frac{8}{3}L_M^2 + \frac{8}{3}t_M^2\right]$$
$$\tilde{C} = \frac{16}{3}\left(\frac{bt_{piezo}^3}{s_{11}}\right)^2 \ .$$

A.4 Derivation of X-Direction Sensitivity

When this system is excited in the x-direction, it does not generate voltage as a result of longitudinal extension/contraction of the beam because of the parallel connection of the piezoelectric layers (positive and negative cancellation). However, an electrical response is generated as a result of the bending motion caused by the location of the center of gravity of the proof mass (below the neutral axis of the beam) in response to x-direction motion. In this case, the boundary conditions defined for each direction of motion are used to solve for

the six coefficients of the transverse ($W(x)$) and longitudinal ($U(x)$) beam motion:

$$W(x) = C_1 \sin(kx) + C_2 \cos(kx) + C_3 \sinh(kx) + C_4 \cosh(kx)$$

$$U(x) = C_5 \sin\left(\frac{\omega}{c}x\right) + C_6 \cos\left(\frac{\omega}{c}x\right) \ .$$

The definition of k can be found in Section 2.3.2, and $c = \sqrt{1/s_{11}\rho_{piezo}}$.

The boundary conditions for the transverse beam motion differ slightly from Eqs. 2.7-2.10. They are the following:

$$W(0) = 0$$

$$\frac{dW(0)}{dx} = 0$$

$$\overline{EI}\frac{d^2W(L)}{dx^2} = \frac{1}{2}ML_M\omega^2 W(L) + I_M\omega^2\frac{dW(L)}{dx} + M\omega^2\left(\frac{t_M}{2} - t_{piezo}\right)U(L) - \frac{bd_{31}t_{piezo}}{s_{11}}V_P$$

$$\overline{EI}\frac{d^3W(L)}{dx^3} = -M\omega^2 W(L) - \frac{1}{2}ML_M\omega^2\frac{dW(L)}{dx} \ .$$

In these equations, $\overline{EI}$ is given in Eq. 2.5 accompanied by other variable definitions. The coupling to the longitudinal response is seen in the $U(L)$ term in the moment boundary condition at $x = L$. Two more boundary conditions are required for the longitudinal solution. The first is the applied motion in the x-direction

$$U(0) = U_b$$

and the second is the force balance with the proof mass at $x = L$

$$\frac{A}{s_{11}}\frac{dU(L)}{dx} = M\omega^2 U(L) + M\omega^2\left(\frac{t_M}{2} - t_{piezo}\right)\frac{dW(L)}{dx}$$

where A is the cross sectional area of the beam and the coupling to the transverse deflection is seen in the second term on the right side of the equation. The final equation in this system is Eq. 2.14, solved for the open-circuit case when $Q_P = 0$.

BIBLIOGRAPHY

BIBLIOGRAPHY

[1] Chittka L. Brockman. Anatomy of the human ear blank. https://commons.wikimedia.org/wiki/File:Anatomy_of_the_Human_Ear_blank.svg, Sept. 2009. License: CC-BY-2.5.

[2] Corinne A. Pittman, Bryan K. Ward, and Carrie L. Nieman. A Review of Adult-Onset Hearing Loss: a Primer for Neurologists. *Current Treatment Options in Neurology*, 23(7), May 2021.

[3] World Health Organization. World report on Hearing. 2021. Licence: CC BY-NC-SA 3.0 IGO.

[4] Gerald R. Popelka, Brian C. J. Moore, Richard R. Fay, and Arthur N. Popper, editors. *Springer Handbook of Auditory Research: Hearing Aids*. Springer International Publishing Switzerland, 2016.

[5] BC Family Hearing. http://www.bcfamilyhearing.com/%20my-child-has-a-hearing-loss/hearing/cochlear-implants/, 2016. License: CC-BY-4.0.

[6] Acoustics - Normal equal-loudness-level contours, 2003. BS ISO 226:2003.

[7] Human ear. https://www.britannica.com/science/ear, Oct. 2020. Accessed: 2021-06-05.

[8] William A. Yost. *Fundamentals of hearing: an introduction*. Academic Press, 3rd edition, 1994.

[9] Anatomy and General Physiology of the Ear. Technical report.

[10] Peter Dallos, Arthur N. Popper, and Richard R. Fay, editors. *Springer Handbook of Auditory Research: The Cochlea*. Springer Seienee+Business Media New York, 1996.

[11] Jonathan P. Fay, Sunil Puria, and Charles R. Steele. The discordant eardrum. *Proceedings of the National Academy of Sciences of the United States of America*, 103(52):19743–19748, Dec. 2006.

[12] G. Volandri, F. Di Puccio, P. Forte, and C. Carmignani. Biomechanics of the tympanic membrane. *Journal of Biomechanics*, 44(7):1219–1236, 2011.

[13] Sunil Puria, Richard R. Fay, and Arthur N. Popper, editors. *Springer Handbook of Auditory Research: The Middle Ear - Science, Otosurgery, and Technology*. Springer Science+Business Media New York, 2013.

[14] Ryuichi Aibara, Joseph T. Welsh, Sunil Puria, and Richard L. Goode. Human middle-ear sound transfer function and cochlear input impedance. *Hearing Research*, 152:100–109, Oct. 2001.

[15] C. Daniel Geisler. *From sound to synapse: physiology of the mammalian ear*. Oxford University Press, 1998.

[16] Stefan Stenfelt and Richard L. Goode. Bone-conducted sound: Physiological and clinical aspects. *Otology and Neurotology*, 26(6):1245–1261, 2005.

[17] Frank R. Lin, John K. Niparko, and Luigi Ferrucci. Hearing Loss Prevalence in the United States. *Archives of Internal Medicine*, 171(20):2011–2012, Nov. 2015.

[18] Adele M. Goman and Frank R. Lin. Prevalence of Hearing Loss by Severity in the United States. *American Journal of Public Health*, 106(10):1820–1822, Oct. 2016.

[19] Quick Statistics About Hearing. https://www.nidcd.nih.gov/health/statistics/quick-statistics-hearing. Accessed: 2020-06-02.

[20] Types and causes of hearing loss. https://www.starkey.com/hearing-loss/types-and-causes. Accessed: 2020-06-02.

[21] Marta Roccio, Pascal Senn, and Stefan Heller. Novel insights into inner ear development and regeneration for targeted hearing loss therapies. *Hearing Research*, 397, Nov. 2019.

[22] Stefan Stenfelt. Middle ear ossicles motion at hearing thresholds with air conduction and bone conduction stimulation. *Journal of the Acoustical Society of America*, 119(5):2848–2858, May 2006.

[23] Sara Lerner. Limitations of Conventional Hearing Aids: Examining Common Complaints and Issues that Can and Cannot Be Remedied. *Otolaryngologic Clinics of North America*, 52(2):211–220, 2019.

[24] Meng Guo. an empirical study on acoustic feedback path across hearing aid users. In *ICASSP 2020 - 2020 IEEE International Conference on Acoustics, Speech and Signal Processing (ICASSP)*.

[25] Matthew L. Carlson, Colin L. W. Driscoll, René H. Gifford, and Sean O. McMenomey. Cochlear implantation: Current and future device options. *Otolaryngologic Clinics of North America*, 45(1):221–248, 2012.

[26] How Cochlear Implants Work. https://www.cochlear.com/us/en/home/diagnosis-and-treatment/how-cochlear-solutions-work/cochlear-implants/how-cochlear-implants-work/how-cochlear-implants-work. Accessed: 2020-05-20.

[27] Fan-Gang Zeng, Arthur N. Popper, and Richard R. Fay, editors. *Springer Handbook of Auditory Research: Cochlear Implants - Auditory Prostheses and Electric Hearing*. Springer-Verlag New York, Inc., 2004.

[28] Florian Denk, Stephan D. Ewert, and Birger Kollmeier. On the limitations of sound localization with hearing devices. *The Journal of the Acoustical Society of America*, 146(3):1732–1744, Sept. 2019.

[29] E S Olson. Direct measurement of intra-cochlear pressure waves [see comments]. *Nature*, 402(6761):526–529, 1999.

[30] Katherine E Knisely. *The Application of a Piezoelectric MEMS Cantilever Array as a Completely Implantable Cochlear Implant*. PhD thesis, 2014.

[31] David S. Haynes, Jadrien A. Young, George B. Wanna, and Michael E. Glasscock. Middle ear implantable hearing devices: an overview. *Trends in Amplification*, 13(3):206–214, Sept. 2009.

[32] Renee M. Banakis Hartl and Herman A. Jenkins. Implantable Hearing Aids: Where are we in 2020? *Laryngoscope Investigative Otolaryngology*, 5(6):1184–1191, Oct. 2020.

[33] Matthew L. Carlson, Stanley Pelosi, and David S. Haynes. Historical development of active middle ear implants. *Otolaryngologic Clinics of North America*, 47(6):893–914, 2014.

[34] Michael D. Seidman, Tyler A. Janz, and Jack A. Shohet. Totally Implantable Active Middle Ear Implants. *Otolaryngologic Clinics of North America*, 52(2):297–309, 2019.

[35] Luca Bruschini, Francesca Forli, Susanna Passetti, Paolo Bruschini, and Stefano Berrettini. Fully implantable otologics MET Carina ™ device for the treatment of sensorineural and mixed hearing loss: audio-otological results. *Acta Oto-Laryngologica*, 130(10):1147–1153, 2010.

[36] Janaina Oliveira Bentivi Pulcherio, Aline Gomes Bittencourt, Patrick Rademaker Burke, Rafael Da Costa Monsanto, Rubens De Brito, Robinson Koji Tsuji, and Ricardo Ferreira Bento. Carina® and Esteem®: A systematic review of fully implantable hearing devices. *PLoS ONE*, 2014.

[37] Knowles. MEMS Microphone MM20-33366-000, Sept. 2019. Datasheet.

[38] Seong Tak Woo, Dong Ho Shin, Hyung Gyu Lim, Ki Woong Seong, Peter Gottlieb, Sunil Puria, Kyu Yup Lee, and Jin Ho Cho. A new trans-tympanic microphone approach for fully implantable hearing devices. *Sensors*, 15(9):22798–22810, Sept. 2015.

[39] Ki Woong Seong, Ha Jun Mun, Dong Ho Shin, Jong Hoon Kim, Hideko Heidi Nakajima, Sunil Puria, and Jin Ho Cho. A vibro-acoustic hybrid implantable microphone for middle ear hearing aids and cochlear implants. *Sensors (Switzerland)*, 19(5), Mar. 2019.

[40] Flurin Pfiffner, Lukas Prochazka, Dominik Peus, Ivo Dobrev, Adrian Dalbert, Jae Hoon Sim, Rahel Kesterke, Joris Walraevens, Francesca Harris, Christof Roosli, Dominik Obrist, and Alexander Huber. A MEMS Condenser Microphone-Based Intracochlear Acoustic Receiver. *IEEE Transactions on Biomedical Engineering*, 64(10):2431–2438, Oct. 2017.

[41] Lukas Prochazka, Alexander Huber, Ivo Dobrev, Francesca Harris, Adrian Dalbert, Christof Roosli, Dominik Obrist, and Flurin Pfiffner. Packaging technology for an implantable inner ear MEMS microphone. *Sensors (Switzerland)*, 19(20):4487, Oct. 2019.

[42] Katherine Knisely, Chuming Zhao, and Karl Grosh. A MEMS AlN transducer array with flexible interconnections for use as a cochlear implant. In *AIP Conference Proceedings*, volume 1703. American Institute of Physics Inc., Dec. 2015.

[43] Chuming Zhao, Katherine E. Knisely, and Karl Grosh. Design and fabrication fo a piezoelectric MEMS xylophone transducer with a flexible electrical connection. *Sensors and Actuators A: Physical*, 275:29–36, Mar. 2018.

[44] Chuming Zhao, Katherine E. Knisely, Deborah J. Colesa, Bryan E. Pfingst, Yehoash Raphael, and Karl Grosh. Voltage readout from a piezoelectric intracochlear acoustic transducer implanted in a living guinea pig. *Scientific Reports*, 9(1), Dec. 2019.

[45] Chuming Zhao. *Ultraminiature Piezoelectric Implantable Acoustic Transducers for Biomedical Applications*. PhD thesis, 2018.

[46] Francis X. Creighton, Xiying Guan, Steve Park, Ioannis Kymissis, Hideko Heidi Nakajima, and Elizabeth S. Olson. An intracochlear pressure sensor as a microphone for a fully implantable cochlear implant. *Otology and Neurotology*, 37(10), 2016.

[47] Steve Park, Xiying Guan, Youngwan Kim, Francis (Pete) X. Creighton, Eric Wei, Ioannis(John) Kymissis, Hideko Heidi Nakajima, and Elizabeth S. Olson. PVDF-Based Piezoelectric Microphone for Sound Detection Inside the Cochlea: Toward Totally Implantable Cochlear Implants. *Trends in Hearing*, 22:233121651877445, 2018.

[48] Woo-Tae Park, Kevin N. O'Connor, Kuan-Lin Chen, Joseph R. Mallon Jr., Toshiki Maetani, Parmita Dalal, Rob N. Candler, Vipin Ayanoor-Vitikkate, Joseph B. Roberson Jr., Sunil Puria, and Thomas W. Kenny. Ultraminiature encapsulated accelerometers as a fully implantable sensor for implantable hearing aids. *Biomedical Microdevices*, 9:939–949, June 2007.

[49] Wen H. Ko, Rui Zhang, Ping Huang, Jun Guo, Xuesong Ye, Darrin J. Young, and Cliff A. Megerian. Studies of MEMS acoustic sensors as implantable microphones for totally implantable hearing-aid systems. *IEEE Transactions on Biomedical Circuits and Systems*, 3(5):277–285, 2009.

[50] Darrin J. Young, Mark A. Zurcher, Maroun Semaan, Cliff A. Megerian, and Wen H. Ko. MEMS capacitive accelerometer-based middle ear microphone. *IEEE Transactions on Biomedical Engineering*, 59(12):3283–3292, Dec. 2012.

[51] M. Sachse, W. Hortschitz, M. Stifter, H. Steiner, and T. Sauter. Design of an implantable seismic sensor placed on the ossicular chain. *Medical Engineering and Physics*, 35(10):1399–1405, 2013.

[52] Xian-Hao Jia, Na Gao, Xin-Da Xu, Yong-Zhen Wu, Hou-Yong Kang, and Fang-Lu Chi. A new floating piezoelectric microphone for the implantable middle ear microphone in experimental studies. *Acta Oto-Laryngologica*, 136(12):1248–1254, July 2016.

[53] A. L. Gesing, F. D.P. Alves, S. Paul, and J. A. Cordioli. On the design of a MEMS piezoelectric accelerometer coupled to the middle ear as an implantable sensor for hearing devices. *Scientific Reports*, 8(1):1–10, Mar. 2018.

[54] Andre Loch Gesing, Zargos Neves Masson, Diego Calero Arellano, Fabio Alves, Stephan Paul, and Julio Apolinario Cordioli. Middle Ear Ossicular Chain Vibration Detection by Means of an Optimized MEMS Piezoelectric Accelerometer. *IEEE Sensors Journal*, 19(6):2079–2086, Mar. 2019.

[55] Robert John Littrell. *High Performance Piezoelectric MEMS Microphones*. PhD thesis, 2010.

[56] F. Martin, P. Muralt, M. A. Dubois, and A. Pezous. Thickness Dependence of the Properties of Highly C-Axis Textured AlN thin films.

[57] Marcus Yip, Rui Jin, Hideko Heidi Nakajima, Konstantina M. Stankovic, and Anantha P. Chandrakasan. A fully-implantable cochlear implant SoC with piezoelectric middle-ear sensor and arbitrary waveform neural stimulation. *IEEE Journal of Solid-State Circuits*, 50(1):214–229, Jan. 2015.

[58] Marcus Yip. *Ultra-low-power Circuits and Systems for Wearable and Implantable Medical Devices*. PhD thesis, 2013.

[59] Hasan Ulusan, Ali Muhtaroglu, and Haluk Kulah. A Sub-500 µW Interface Electronics for Bionic Ears. 7:132140–132152, Sept. 2019.

[60] Bosch Sensortec. BMA456 - Data Sheet: Digital, triaxial acceleration sensor, 2019. Technical reference code: 0 273 141 282.

[61] TE Connectivity. 820M1 Condition Monitoring Accelerometer, 2019.

[62] Vesper Technologies. VA1200 Piezoelectric MEMS Voice Accelerometer with Analog Output, 2020. Datasheet.

[63] Diego Calero, Stephan Paul, André Gesing, Fabio Alves, and Júlio A. Cordioli. A technical review and evaluation of implantable sensors for hearing devices. *BioMedical Engineering Online*, 17(1):1–26, 2018.

[64] Oticon Medical. Neuro 2 - Where sound meets design.

[65] Don A. Berlincourt, Daniel R. Curran, and Hans Jaffe. *Piezoelectric and Piezommagnetic Materials and Their Function in Transducers*, volume 1, chapter 3, pages 170–270. Academic Press Inc., 1964.

[66] S. Trolier-Mckinstry and P. Muralt. Thin film piezoelectrics for MEMS. *Journal of Electroceramics*, 12:7–17, 2004.

[67] Katherine Knisely and Karl Grosh. Effect of AC target power on AlN film quality. *Journal of Vacuum Science & Technology A: Vacuum, Surfaces, and Films*, 32(5):51504, 2014.

[68] Gustav Gautschi. *Piezoelectric Sensorics Force Strain Pressure Acceleration and Acoustic Emission Sensors Materials and Amplifiers*. Springer Berlin Heidelberg: Imprint: Springer, 2002.

[69] Michael Krommer. On the correction of the Bernoulli-Euler beam theory for smart piezoelectric beams. *Smart Materials and Structures*, 10:668–680, 2001.

[70] Robert Littrell and Karl Grosh. Modeling and characterization of cantilever-based MEMS piezoelectric sensors and actuators. *Journal of Microelectromechanical Systems*, 2012.

[71] Nidhi Gupta, Akhilesh Pandey, Siva Rama Krishna Vanjari, and Shankar Dutta. Influence of residual stress on performance of AlN thin film based piezoelectric MEMS accelerometer structure. *Microsystem Technologies*, 25(10):3959–3967, Feb. 2019.

[72] Felix A Levinzon. Fundamental Noise Limit of Piezoelectric Accelerometer. 4(1):108–111, 2004.

[73] Don L. Devoe and Albert P. Pisano. Modeling and Optimal Design of Piezoelectric Cantilever Microactuators. *Journal of Microelectromechanical Systems*, 6(3):266–270, Sept. 1997.

[74] Alison E. Hake, Chuming Zhao, Wang-Kyung Sung, and Karl Grosh. Design and Experimental Assessment of Low-Noise Piezoelectric Microelectromechanical Systems Vibration Sensors. *IEEE Sensors Journal*, 2021.

[75] Keysight Technologies. *User's Guide Keysight E4980A/AL Precision LCR Meter*.

[76] Alison E. Hake, Chuming Zhao, Lichuan Ping, and Karl Grosh. Ultraminiature AlN diaphragm acoustic transducer. *Applied Physics Letters*, 117(14):143504, Oct. 2020.

[77] Richard L. Goode, Geoffrey Ball, Shinsei Nishihara, and Koshiro Nakamura. Laser Doppler vibrometer (LDV) - A new clinical tool for the otologist. *American Journal of Otology*, 17(6):813–822, 1996.

[78] S. M. Shahruz. Design of mechanical band-pass filters with large frequency bands for energy scavenging. *Mechatronics*, 16(9):523–531, Nov. 2006.

[79] Haifeng Zhang and Karim Afzalul. Design and analysis of a connected broadband multi-piezoelectric-bimorph- beam energy harvester. *IEEE Transactions on Ultrasonics, Ferroelectrics, and Frequency Control*, 61(6):1016–1023, June 2014.

[80] Waleed Al-Ashtari, Matthias Hunstig, Tobias Hemsel, and Walter Sextro. Enhanced energy harvesting using multiple piezoelectric elements: Theory and experiments. *Sensors and Actuators, A: Physical*, 200:138–146, Jan. 2013.

[81] Shaofan Qi, Roger Shuttleworth, S. Olutunde Oyadiji, and Jan Wright. Design of a multiresonant beam for broadband piezoelectric energy harvesting. *Smart Materials and Structures*, 19(9), Aug. 2010.

[82] R. M. Toyabur, M. Salauddin, and Jae Y. Park. Design and experiment of piezoelectric multimodal energy harvester for low frequency vibration. *Ceramics International*, 43:S675–S681, Aug. 2017.

[83] Robert David White. *Biomimetic Trapped Fluid Microsystems for Acoustic Sensing*. PhD thesis, University of Michigan, 2005.

[84] Robert D White, Robert Littrell, and Karl Grosh. A Microscale Bioinspired Cochlear-like Sensor. In *Microfluidic Technologies for Human Health*. World Scientific Publishing Company, 2012.

[85] Jongmoon Jang, JangWoo Lee, Seongyong Woo, David J Sly, Luke J Campbell, Jin-Ho Cho, Stephen J O'Leary, Min-Hyun Park, Sungmin Han, Ji-Wong Choi, Jeong Hun Jang, and Hongsoo Choi. A microelectromechanical system artificial basilar membrane based on a piezoelectric cantilever array and its characterization using an animal model. *Scientific Reports*, 5:12447, July 2015.

[86] Mark Bachman, Fan Gang Zeng, Tao Xu, and G. P. Li. Micromechanical resonator array for an implantable bionic ear. *Audiology and Neurotology*, 11(2):95–103, Jan. 2006.

[87] Second Order and Higher Order Systems. http://engineering.ju.edu.jo/Laboratories/05%20-%20Second%20Order%20System%20and%20Higher%20order.pdf.

[88] Singiresu S. Rao. *Mechanical Vibrations*. Addison-Wesley Publishing Company Inc., 3rd edition, 1995.